Characterization of a new type of nanoparticle generator for medical inhalation applications

A Master Thesis Project in Aerosol Technology

Author: André Nagy
Examiner: Joakim Pagels
Supervisor: Jakob Löndahl

Abstract

A new type of nanoparticle generator is being developed at Lund University. This project aimed to characterize it in order to produce a stable aerosol for medical inhalation applications. This project characterized size distributions during different parameter settings for the generator. The experimental work included assessing the effect of cleaning the generator between experiments for experimental runs all between 2 and 22 hours a piece. Other factors such as source material consumption and the effect of adjusting the different flows and temperatures were also investigated. Although that the results show mode switching it was found that a stable number concentration is possible for up to at least 20 hours and delivers nanoparticle within the range of 10-200 nanometers. Thus, with correct settings the generator satisfy the requested criteria to produce nanoparticles suitable for inhalation.

Acknowledgements

Contents

List of Figures

List of Tables

1 Introduction

1.1 Background

A general nanoparticle generator can be used for many different types of applications, however a desirable function that is not yet available on the market is the ability to generate organic nanoparticles suitable for inhalation. A major obstacle with current commercial versions of particle generators on the nanoscale is that there is an abundance of impurities, such as for example soot particles which are not suitable for inhalation. This inability to specify the amount and account for all eventual impurities hinders them from being used in for medical applications. [2]

A generator for organic nanoparticles has been under development at Lund University since around 2013, it generates aerosolized particles by evaporation in an oven and then condensation in a cooling chamber. There are four primary variables which controls the concentration and the size distribution, these are: the cooling chamber temperature (T_C), the oven temperature (T_H), the cooler dilution flow (Q_C) and the gas supply flow (Q_H). In addition to these continuously adjustable variables one can also change the type of source material, supply gas and the size/geometry of the sample holding cup among other things.

1.2 Problem Description and Aims

The general aim with the generator that is investigated and developed in this thesis is to be able to generate nanoparticles in an aerosol suitable for inhalation in accordance with state departments such as the swedish 'Läkemedelsverket' or the american 'Food and Drug Administration'.

The specific aim with this project is to investigate the stability of the generator in terms of how the aforementioned variables affect the number concentration and size distribution of the generated aerosol. As well as determine stable parameter settings with respect to the reproducibility of a desired number concentration and size distribution. The desired number concentration is typically in the range of a million particles per cubic centimeter and the desired size distribution is a relatively monodisperse distribution centered around 50 nm with particles no larger than 100 nm.

In order to fulfill this goal a number of experiments were done such as:

- Measuring source material consumption.
- Evaluating the effect of cleaning the generator.
- Observing the number concentration over long periods of time.
- Adjusting the four different parameters to see their respective effect on the number concentration and size distribution of the aerosol.

1.3 Structure of the Report

The section of background and theory is meant to provide sufficient background knowledge and theory as to how different methods and theoretical systems apply to what is being described in the methodology as well as the discussion.

The section on methodology shows the experimental setup, which is presented with each of the technical instruments and a description of the generator. Then the different stages of ex-

1

perimental work is overviewed such as a description on what makes a good source material and the approach on how to investigate important characteristics of the generator.

The results section is divided into the main experimental subsections. Such as source material consumption, how the number concentration of aerosol and snapshots of the size distribution behaves when not cleaning the generator in between each run, or when it is cleaned. As well as long time series trying to reproduce a stable concentration but for a long time. Then a subsection for measurement series with respect to the different adjustable parameters.

The discussion will include observations and interpretations on what is being presented in the results section. All interesting or unexpected phenomena arising from experiments will be lifted and discussed. It will include different hypotheses and suggestions on how to approach eventual problems.

Lastly an evaluation on what has been done throughout the course of the project will be presented. I will discuss whether the results hold inherent value or if they are dismissible.

2 Background & Theory

2.1 Nanoparticles and Lung Deposition

Upon inhalation of a polydisperse aerosol the respiratory tract allows for certain particles to reach different parts of it, which mainly depends on the size of the particle. There are generally three different types of mechanisms that determine respiratory deposition, i.e. inertial impaction, gravitational sedimentation and diffusion. The mechanisms in concurrence with the particle size determine in which part of the respiratory tract the deposition occurs. Impaction typically occurs for coarse particles, i.e. particles larger than 3000 nm, which mainly happens in the upper respiratory tract. The gravitational settling is mostly relevant in the randomly oriented airways of the lower respiratory tract, where small flow velocities and long residence time leads to sedimentation of particles between 300 and 3000 nm. Diffusion occurs for particles with a diameter smaller than 300 nm, the smallest particles ($d_p \leq 10$ nm) have such a high diffusion velocity that they tend to deposit in the head airways and in the trachea before making any progress down to the deeper levels of the tract. Particles sized between 30 and 300 nm deposit in the alveolar region above any other region. [3]

Nanoparticle is a word that is thrown around a lot. It is usually defined as a particle which has a diameter on the order of 1 to 100 nm. These particles are also often named "ultrafine particles", abbreviated $PM_{0.1}$, which stands for particulate matter with an aerodynamic diameter of up to 100 nm. [4]

Of all these definitions and terms, we are interested in particles that operate in the diffusion-dominated regime. The deposited fraction with respect to particle size and type of deposition mechanism can be seen in Figure 2. Looking at the curve describing alveolar deposition, as well as recognizing the fact that very small particles diffuse in the extrathoracic region, it is apparent that the diffusion dominated regime encompasses particle sizes up to about 300 nm. [5] The upper size limit can be determined by looking at the size in which the deposited fraction by diffusion is matched against the combined deposition fractions by sedimentation and impaction. The main factors in the diffusion-dominated regime with respect to lung deposition are particles mobility size, breathing pattern, morphology of the lungs and hygroscopicity. Important nanoparticle properties, with regards to their interaction with the lungs after deposition are numerous. However some of the most important properties are size, shape, solubility, surface area and surface reactivity as well as chemical composition.

Inhaled aerosol particles have many applications and one is in scintigraphy of the lungs. Scintigraphy is a collective term for all types of diagnostic tests where radiopharmaceuticals are used to target specific organs or tissue, where upon reaching its destination the emitted radiation is detected and then used to form images. Lung scintigraphy is a procedure which uses ventilation- and perfusion scintigraphy to assess pulmonary and cardiovascular disorders, it is also known as 'ventilation/perfusion lung scan' (or V/Q lung scan for short). Aerosol ventilation scintigraphy records the distribution of a radioactive aerosol within the lungs whereas the pulmonary perfusion scintigraphy records the distribution of arterial blood flow. [6]

There are multiple indications for lung scintigraphy, e.g. to see if the patient has pulmonary embolism, observe pulmonary functions before surgery for lung cancer, and evaluate lung transplants among other things. [7]

The most commonly used radiopharmaceutical for lung scintigraphy is ^{99m}Tc - diethylenetri-aminepentaaceatic acid (DTPA). It is administered as an aerosol inhaled by the patient, and the dose received in the lungs is approximately 20-40 MBq.
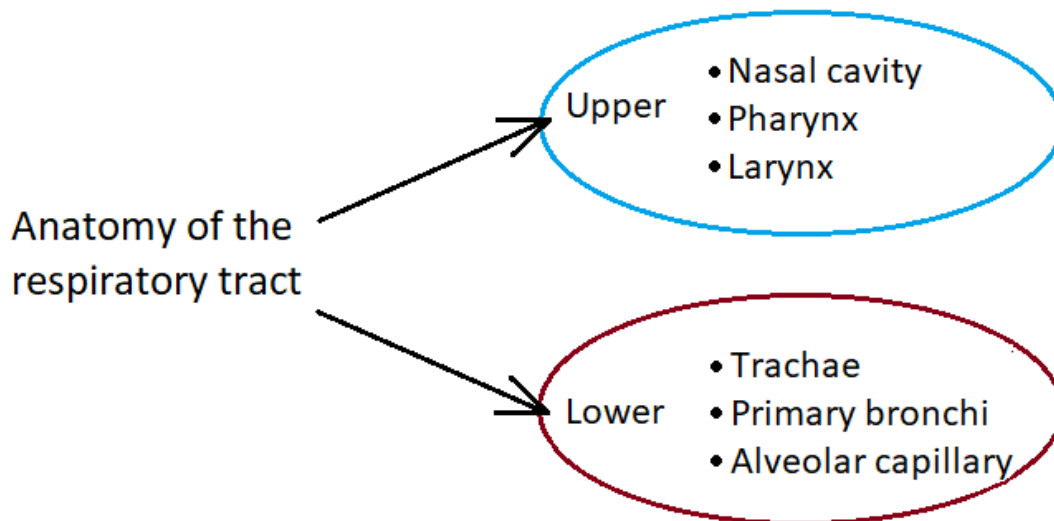
Figure 1: Conducting passages.
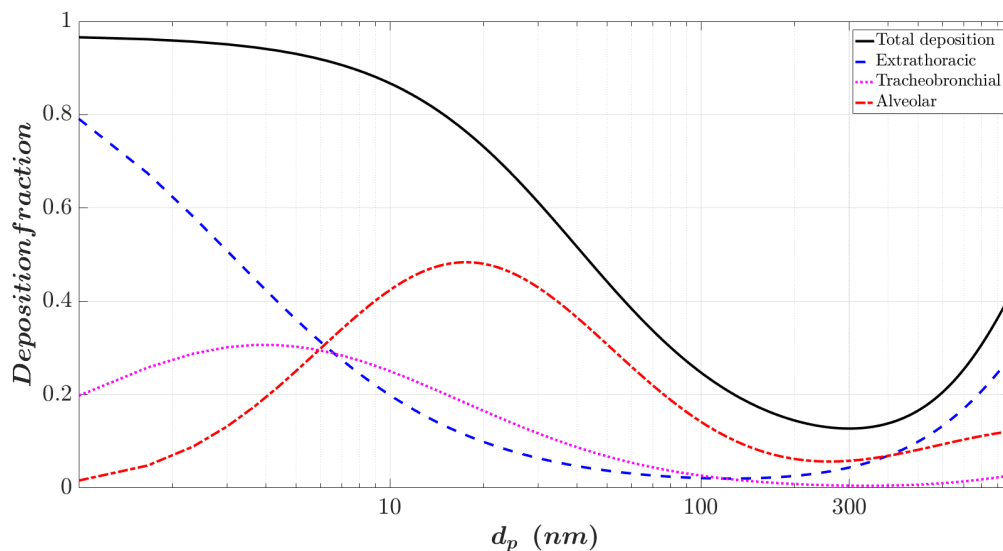
Figure 2: Total and regional deposition according to the ICRP model.

2.2 Particle Generation

There are a number available techniques for producing nanoparticles. The techniques differs in many ways, which will be presented below. Many of the methods does not produce particles with a specific enough size distribution, and/or also produce unwanted bi-products. The wide variety of methods can be illustrated by mentioning that nanoparticles can be generated by pure attrition in ball mills, out of pyrolysis, as well as through simple condensation.

2.2.1 Spark Discharge Generator

The spark discharge generator (SDG) produces particles by generating a spark between two electrodes, which holds an electrical potential. The resulting particles are transported by an

inert gas and filtered through some type of impaction device. The material of the electrodes will determine the type of particles produced, which means that this method is not suitable for generating organic aerosols due to the low number of relevant organic electrodes as well as high spark temperatures that would change the chemistry. [8]

2.2.2   Electrohydrodynamic Atomisation

Electrohydrodynamic atomisation (EHDA), also called electrospraying, refers to the method where a high voltage is applied to a conductive liquid. There are different types of modes for electrospraying, but the most important is known as the 'cone-jet mode'. The liquid is emitted through a nozzle of the apparatus and forms a jet stream, irregularities in the jet lead to the formation of charged particles. One of the major drawbacks of this method is the introduction of impurities, as with any other method that includes liquids. [9]

2.2.3   Spinning Disc Generator

A spinning disc generator works by feeding a suspension or solution onto the center of a rotating disc. When rotating, the liquid is spun of the disc in two groups of droplet sizes, primary (larger) and satellite (smaller). The primary droplets are homogeneous while the satellite droplets are much more numerous and heterogeneous in size. The satellite droplets are removed from the main air stream via a separate exhaust system. However, the typical sizes which are produced are typically larger than 1 to 10 μm. [10]

2.2.4   Evaporation-Nucleation-Condensation

The method of 'evaporation nucleation condensation' (ENC) is a self-described method of aerosol production. The processes involved are typically: nuclei production, vapor generation, vapor-nuclei mixing and condensation with the help of a carrier gas. [11] A source material is evaporated until supersaturation is achieved, the gas is then cooled to condense the vapor molecules. The generated nuclei then grow by condensation onto their surface and coagulation among the particles. [12] [13]

Evaporation generally decreases the particle size because of loss of surface atoms or molecules, in contrast to condensation which increases the particle size by letting atoms or molecules suspended in the gas join the existing particles. [14]

2.2.5   Coagulation

Aerosol coagulation is a process described by how particles collide with each other and in some cases stick to each other. This effectively lowers the number concentration while at the same time shifts the size distribution towards larger values. An almost pure coagulation mode stems from primary particles as seen in Figure 3. There are two main processes which is responsible for coagulation, either through the random movement of particles that results in Brownian coagulation. The relative motion can also be induced due to external sources such as electrical forces or from aerodynamic effects, this is known as kinematic coagulation. [15]

Turbulence is one of the factors that affect the coagulation rate. It can affect coagulation by driving collisions between particles in two different ways. Either by the difference in velocities of polydisperse particles or through the shearing motion of the gas induced by turbulent acceleration. [16]

Besides how the main processes affect coagulation an important fact is that the rate of coagulation is proportional to the square of the number concentration of the aerosol.
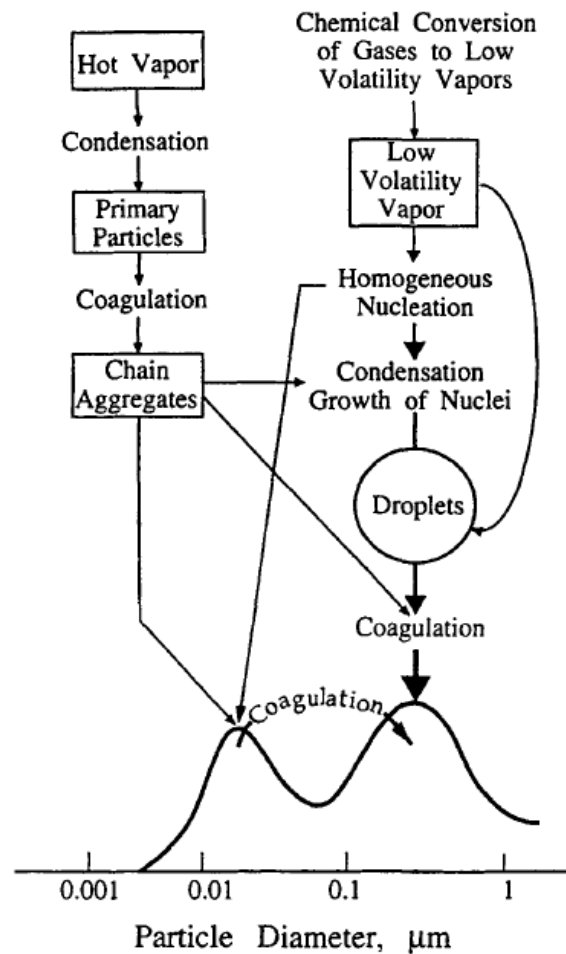
Figure 3: Idealized schematic of the distribution of particle nucleation and growth. [1]

2.3 Particle Size Distribution Statistics

The most common aerosol size distribution is the lognormal distribution. There are multiple reasons for choosing the lognormal distribution over the normal distribution. Empirical data suggests that the lognormal distribution fits better due to the nature of aerosol samples. They often span multiple orders of particle size and have a tendency to be skewed towards the larger particles. [17]

2.3.1 The Lognormal Distribution

The lognormal distribution has advantages such as; enabling the possibility of easy comparison of different modes in the distribution and achieving attainableness of a continuous distribution function. It is also a very simple method to describe a mode, as it is done by only three parameters: geometrical mean diameter (GMD, or here d_g), the geometric standard deviation (GSD, or here σ) and the number of particles (N). Before analyzing the data, the particle size range is divided into 'bins'. This lets us see how many counts in each particle size interval as

well as logarithmize the width of a size interval, this is seen as in Equation 1,

$$\Delta \log d = \log d^h - \log d^l \tag{1}$$

where d is the particle diameter and the superscript h and l marks the higher and lower interval value for each bin.

The lognormal distribution function can be represented as seen in Equation 2,

$$\frac{\Delta N}{\Delta \log d} = \frac{N}{\sqrt{2\pi} \log \sigma} \exp\left(-\frac{(\log d - \log d_g)^2}{2(\log \sigma)^2}\right), \tag{2}$$

where the aforementioned three parameters is defined as in Equation 3, 4 and 5,

$$d_g = \exp\left(\frac{\sum_i \Delta N_i \log d_i}{N}\right) \tag{3}$$

$$\sigma = \exp\left(\frac{\sum_i \Delta N_i (\log d_i - \log d_g)^2}{N-1}\right)^{-\frac{1}{2}} \tag{4}$$

$$N = \sum_i \Delta N_i, \tag{5}$$

for i number of bins. [17]

2.3.2 Multiple Modes

For data fitting multiple lognormal modes, one simply writes the sum of multiple lognormal distribution functions. This is done as seen in Equation 6, where $f(d)$ is the sum of n number of particle modes:

$$f(d) = \frac{\Delta N}{\Delta \log d} = \sum_n \frac{N_n}{\sqrt{2\pi} \log \sigma_n} \exp\left(-\frac{(\log d - \log d_{g,n})^2}{2(\log \sigma_n)^2}\right), \tag{6}$$

For a size distribution with n modes, to accurately describe the data, 3n parameters are needed. These parameters are given by using a mathematical fitting method on the data.

2.3.3 Multimodal Lognormal Data Fitting

A method for fitting the data is the nonlinear least squares estimation method (NLSE).

$$\min_d ||f(d)||_2^2 = \min_d \left(f_1(d)^2 + f_2(d)^2 + \cdots + f_n(d)^2\right) \tag{7}$$

A nonlinear least squares regression method make use of iterative optimization procedures, which in turn requires an estimated starting value d_0 for the unknown parameters. The estimated starting values needs to be fairly close to the actual value, or the optimization procedure may not converge. One can also specify lower and upper bounds d_{min} and d_{max}, so that the solution always is in the range of $d_{min} \leq d \leq d_{max}$.

The unknown values of the parameters are estimated by finding numerical values of the parameters which minimize the sum of squares, i.e. the euclidean norm between each observed response and its fitted value. To minimize $||f(d)||_2^2$, a generic algorithm can be written as in Equation 8,

$$d^{(i+1)} = d^{(i)} + s^{(i)} v^{(i)} \tag{8}$$

where the $(i+1)^{th}$ iterated value of $d^{(i+1)}$ is obtained from the previous iteration $d^{(i)}$ by regulating the term $s^{(i)} v^{(i)}$, where $s^{(i)}$ controls the amount of change and whereas $v^{(i)}$ controls the direction of change. [18]

The first-order Taylor's expansion of $f(d)$ about $d^\dagger$ can be written as seen in in Equation 9,

$$f(d) \approx f(d^\dagger) + [\nabla_d f(d^\dagger)]'(d - d^\dagger) \tag{9}$$

replacing d with $d^{(i+1)}$ and $d^\dagger$ with $d^{(i)}$ we get Equation 10,

$$f(d^{(i+1)}) \approx f(d^{(i)}) + [\nabla_d f(d^{(i)})]' s^{(i)} v^{(i)} \tag{10}$$

which is true when $d^{(i+1)}$ is in the neighborhood $d^{(i)}$. Let $g(d)$ denote the gradient vector of f, $\nabla_d f(d)$, and $g^{(i)}$ denote $g(d)$ evaluated at $d^{(i)}$. If $v^{(i)} = -g^{(i)}$ we get Equation 11,

$$f(d^{(i+1)}) \approx f(d^{(i)}) - s^{(i)} [g^{(i)'} g^{(i)}] \tag{11}$$

One may want to choose $s^{(i)}$ such that the next value of the function $f(d^{(i+1)})$ is a minimum. Which implies that the first order condition seen in Equation 12 should hold,

$$\frac{\delta f(d^{(i+1)})}{\delta s^{(i)}} = \nabla_d f(d^{(i+1)}) \frac{\delta d^{(i+1)}}{\delta s^{(i)}} = -g^{(i+1)'} g^{(i)} = 0 \tag{12}$$

Let $\Gamma^{(i)}$ denote the Hessian matrix of $f(d)$ evaluated at $d^{(i)}$ as seen in Equation 13,

$$\Gamma^{(i)} = \nabla_d^2 f(d) \Big|_{d=d^{(i)}} = \nabla_d g(d) \Big|_{d=d^{(i)}} \tag{13}$$

Then by Taylor's expansion of g, as in Equation 14,

$$g^{(i+1)} \approx g^{(i)} + \Gamma^{(i)} (d^{(i+1)} - d^{(i)}) = g^{(i)} - \Gamma^{(i)} s^{(i)} g^{(i)} \tag{14}$$

Which can be written as seen in Equation 15, because of the relationship stated in Equation 12 ; $g^{(i+1)'} g^{(i)} = 0$,

$$0 = g^{(i+1)'} g^{(i)} \approx g^{(i)'} g^{(i)} - s^{(i)} g^{(i)'} \Gamma^{(i)} g^{(i)} \implies s^{(i)} = \frac{g^{(i)'} g^{(i)}}{g^{(i)'} \Gamma^{(i)} g^{(i)}} \tag{15}$$

By substituting $s^{(i)}$ in Equation 8 as well as recognizing $v^{(i)} = -g^{(i)}$, we now have a full expression of the iterative algorithm as seen in Equation 16,

$$d^{(i+1)} = d^{(i)} - \frac{g^{(i)\prime}g^{(i)}}{g^{(i)\prime}\Gamma^{(i)}g^{(i)}}g^{(i)} \tag{16}$$

To summarize the algorithm it is easily viewed in the four following steps:

1. **Initialization:** Pick a point d_o as an initial guess.
2. **Gradient:** Compute the gradient at your current guess: $v^{(i)} = \nabla_d f(d^{(i)})$.
3. **Update:** Move by your step size $s^{(i)}$ in the direction of the gradient: $d^{(i+1)} = d^{(i)} - s^{(i)}v^{(i)}$.
4. **Iterate:** Repeat steps 1-3 until your function is close enough to zero. (Until $f(d^{(i)}) < \epsilon$, for some small tolerance ϵ).

2.3.4 Particle Growth

The most important aspects of manipulation of particle growth with respect to the resulting aerosol product are the size distribution and the mean particle size. [19] The size distribution of a produced aerosol needs to be narrow for the medical applications of relevance. A monodisperse aerosol is defined to have a geometric standard deviation (GSD) less than 1.25. [20]

The mean particle size only depends on two parameters, the number of nuclei and the degree of supersaturation. If all vapour is used for aerosol formation Equation 17 can be used to calculate the median particle diameter.

$$\bar{d} = \left[\frac{M_G - M_W - M_R}{c_N \rho \frac{\pi}{6}} \right]^{1/3} \tag{17}$$

where $\bar{d}$ is the median particle diameter, M_G is the mass of the vapour at the beginning of the condensation tube, M_W is the mass of the vapour condensing at the walls, M_R is the mass of the vapour at the end of the condensation tube, c_N is the number of condensation nuclei and ρ is the liquid density of the material. [19]

Supersaturation is a state of e.g. a gas that contains more foreign atoms or molecules than it ordinarily can hold at a given temperature and still be thermodynamically stable , and the degree of supersaturation will affect how much condensation that occurs. The air that is containing vapor of our source material will upon cooling achieve a state of supersaturation, and with the presence of nuclei these acts as sites for very small droplets to appear on them. The rate of condensation depends on how supersaturated the air is as much more available material will be ready to condense. [21]

2.4 Fluid Dynamics/Mechanics

The flow of a fluid can generally be described to be either turbulent or laminar. The turbulent flow is characterized by randomness, eddies and recirculation. When none of these properties are shown the flow is said to be laminar.

Turbulent fluid motion is best described as the conditions where quantities such as velocity and pressure varies randomly with time and space. These fluctuations can be induced in different ways, such as the roughness of adjacent surfaces or just general disturbances in the flow. The Reynolds number (Re), which describes the ratio of the inertial to the viscous forces in a fluid, can be used to describe whether laminar or turbulent flow is occurring. At low values the flow

is laminar and after a critical value (Re = 2100) the flow can be said to be both laminar and turbulent up to the second critical value (Re = 4000), after this point the flow is turbulent.

Turbulence can be categorized either as homogeneous, isotropic or anisotropic turbulence. [22]

- Homogeneous turbulence indicates that the velocities are invariant wherever you look in the system.
- Isotropic turbulence is by definition always homogeneous and it describes a system where the quantities have no directional preference.
- Anisotropic turbulence describes a system where the velocities have a directional preference.

Eddies are the swirls that are created when a fluid flows past an obstacle and generates a reverse current, which eventually makes a loop. The size of the smallest eddies is equal to Kolmogorovs length scale η and is defined as in Equation 18,

$$\eta = \left(\frac{\nu^3}{\epsilon} \right)^{1/4} \tag{18}$$

where ν is kinematic viscosity of the fluid and ϵ is the rate of conversion of turbulence into heat by viscosity (aka. the dissipation rate).

2.4.1 Dynamical Regime

An aerosol can generally be described by the dynamical behaviour of the particles as per which 'regime' the particles are classified under. This is size dependent according to the Knudsen number K_n seen in Equation 19,

$$K_n = \frac{2\lambda}{d} \tag{19}$$

where λ is the mean free path of the gas and d is the diameter of the particles.

If $K_n >> 1$ the particles are very small compared to the mean free path of the suspending gas. The aerosol is then said to operate under the 'free molecular regime' where the particles act similarly to large gas molecules and tend to follow streamlines of the flow while at the same time undergo fast Brownian diffusion. But when $K_n << 1$ we are operating under 'continuum flow regime' where particles are in a viscous flow under the works of continuum mechanics. In our case the mean free path $\lambda \approx 65$ nm, which puts us with a Knudsen number at $0.1 < K_n < 10$, which is to say that we are working with under the 'transition regime', which means that the flow is neither viscous nor molecular.

3 Methodology

The general setup can be viewed in Figure 4, which shows the simplicity of the system. There are two flows which connects from a pressure system to the generator. The oven and the cooler part of the generator each receives an individual flow. The oven and cooler is controlled by two different elements that sets their individual temperatures. The output of the generator is connected to a scanning mobility particle sizer (which measures the size and number of particles) that is in conjunction with a computer that produces the size distribution data files.

3.1 Experimental Setup

Before each experimental session a couple of possibilities are presented, e.g., which cup we want to use and which nozzle to use for the connection between the oven and cooling chamber. However, after doing some trial runs with different sizes, the nozzle and cup size for all experiments presented in this project can be seen in Table 2.

Each flow rate variable is checked with a flow-meter, the only variable which will differ some from experiment to experiment whether we want to or not is the flow-rate $Q_{Aerosol}$. However, it never dips lower than a value of 0.98 lpm or exceeds a value higher than 1.06 lmp.
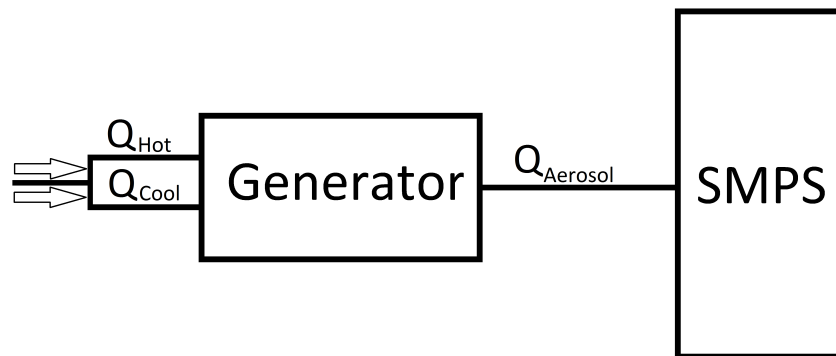
Figure 4: The experimental setup where Q_{Hot} is the oven flow, Q_{Cool} is the cooler flow and $Q_{Aerosol}$ is the flow of the resulting aerosol.

In Figure 4 a simplified schematic is shown to give a better overview over the experimental setup. In this picture the scanning mobility particle sizer (marked SMPS) encompasses all relevant instruments such as a differential mobility analyzer (which measures the size of a particle), condensation particle counter and a computer for data analysis. Before each session, the condensation particle counter (which counts the number of particles at a certain size) must be checked to make sure there are enough butanol for the entire run, the particle free sheat flow Q_{sheat} (which sets the differential mobility analyzer to operate correctly) is adjusted to have a value of 7.00 lpm. While waiting for the condensation particle counter to warm up the sample is weighed to determine the last sessions consumption as well as the amount of matter present for the actual experiment.

3.1.1 The Generator

The generator consists mainly of two sections, the evaporation section (or oven) which consists of a PTC element (that is a positive temperature coefficient heater element) together with a chamber, and the nucleation section (or cooler) which consists of a Peltier element together

with another chamber. The heating- and the cooling- compartment are regulated individually through their respective micro-computer controller.

3.1.2 Scanning Mobility Particle Sizer

The scanning mobility particle sizer (SMPS) is used to determine the size distribution and the number concentration of aerosol particles. The SMPS system consists mainly of a differential mobility analyzer (DMA), a condensation particle counter (CPC) and a computer.

The aerosol sample begins its flow path by going through an impactor to remove large particles. Thereafter it is neutralized through a bipolar ion neutralizer to bring the aerosol samples charge level to a steady state. Next the sample flows through the differential mobility analyzer (DMA) that separates the particles according to their electrical mobility. The selected particles are transported to the condensation particle counter (CPC) which measures the number concentration of the aerosol sample.

3.1.2.1 Differential Mobility Analyzer

The DMA is based of the principle that the capability of a particle to cross an electrical field is related to the particle diameter, i.e. the electrical mobility Z, which is inversely proportional to the particle diameter d_p as seen in Equation 20. [23]

$$Z = \frac{n_p e C}{3 \pi \eta d_p} \tag{20}$$

Where n_p is the number of charges per particle, e is the elementary unit of charge, C is the Cunningham slip correction, η is the viscosity of the gas and d_p is the particle diameter.

3.1.2.2 Condensation Particle Counter

A CPC is used to count the number of particles in an aerosol, which is done by letting the particles travel through a laser. That means they need to be at least a size where it can be optically detected. The enlargement of the particles is done by first letting them travel through a chamber filled with a supersaturated gas, in our case butanol, where condensation occurs using the particles as nucleation centers. [24]

3.2 Automation of Temperature Control

3.2.1 PID Controller

The micro controller uses the 'proportional integral derivative' (PID) feedback mechanism. The controller continuously calculates the difference between the main set value known as SV, and the process variable known as PV(t), this difference is known as the error value e(t).

The controller aims to reduce the error value to zero, which is done by tuning the control variable u(t). This correction is based on proportional, integral and derivative terms as shown in Equation 21,

$$u(t) = K_p e(t) + K_i \int_0^t e(t)dt + K_d \frac{de(t)}{dt} \tag{21}$$

where K_p, K_i and K_d are the coefficients of the proportional, integral and derivative terms respectively.

· K_p adjusts for present values of the error.
· K_i adjusts for past values of the error.
· K_d adjusts for probable future values of the error.

3.2.2 PID Tuning

The micro-computer controlling the heating- and cooling elements is tuned to achieve a stable temperature where a fluctuation of 0.4 degrees celsius is allowed. The proper coefficients for K_p, K_i and K_d was first chosen by using the 'step response method', however the calculated values resulted in a large temperature fluctuation. The 'Ziegler–Nichols tuning method' turned out to give a good temperature stability. These values are shown in Table 1.

Table 1: Control coefficients.

Element	K_p	K_i	K_d
Heater	4	17	4
Cooler	0,4	27	7

3.3 Curve Fitting

The size distribution data collected with the SMPS comes as a matrix in a text document, which is imported into MATLAB. The data points are sorted out in a number of necessary arrays. For example arrays that represent the size bins, or the concentration over each individual bin, as well as the total concentration over time for each experimental run. The sizes are logarithmized and differentiated according to Equation 1.

Multiple snapshots in time of the size distribution were chosen and are marked as seen in for example Figure 34. The size distributions are then loaded by a script that handles the data fitting according to the methodology explained in Section 2.3.3.

3.4 Source Material Consumption

Due to a non-disclosure agreement I will not list what material is used for aerosolization, and will call it 'compound A'. The source material was chosen with a few abilities in mind, such as it should be balanced with respect to its volatility in the temperature range that our generator works well in. It should be non-volatile enough so the particles doesn't evaporate immediately on inhalation, it has to be stable on a timescale of minutes as a nanoparticle but I should also be able to evaporate below 200 °C. Other important attributes is that we are working with a hydrophobic as well as a non-toxic material.

In order to examine the consumption of compound A, the cup with the source material was weighed before and after each run.

3.5 Stability

To determine the so called 'standard set' of variables with respect to stability, the two different flow- (Q_{hot} and Q_{cool}) and temperature- (T_{hot} and T_{cool}) parameters will be changed to see how they affect the aerosol concentration and size distribution.

Upon operating with different values and reviewing some old results, the values in Table 2 was shown to give the desired stability.

Table 2: Parameter settings.

Q_{hot}	Q_{cool}	T_{hot}	T_{cool}	d_{nozzle}	d_{cup}
(lpm)	*(lpm)*	*(°C)*	*(°C)*	*(cm)*	*(cm)*
0.05	1.20	125	16	0.2	2.0

The second set of options with respect to the generator includes choices of nozzle size as well as the geometry and size of the cup, which holds the raw material. The nozzle size is chosen to be 2 mm and the chosen cup is geometrically flat with an outer diameter of 2 cm. Lastly the aerosol flow Q_{aero} is measured and noted before each and every experimental run. These can be seen in Table 4 found in the Appendix.

3.6   Effect of Cleaning the Generator

Up until the standard set of variables were found for stable production, each experimental session was preceded by a thorough cleaning of both the cooling chamber as well as the oven. This was done by washing with ethanol and then using compressed air to remove any remaining residual particles. A heat gun was used if there were an unusual large amount of residuals.

In order to determine whether the need for cleaning in between each session was needed, a series of runs were also carried out without any cleaning using the settings mentioned in Table 2. Afterwards additional runs were done using the same configuration but with one thorough cleaning in between each run.

3.7   Reproducing Stable Concentrations Over Long Time

An important aspect of the applicability of the generator is how long we can run it while maintaining a stable high enough concentration. This was tested once during the measurement series when not cleaning the generator in between runs, but in order to raise the chance of reproducibility the generator was cleaned in between runs. The three experiments were run for a duration of 14, 19 and 22 hours.

3.8   Parameter Adjustment

To observe the stability and subsequently the sensitivity of the generator with respect to the four standard variables, a collection of measurements series were done. So starting at one of the four 'standard set' parameters and proceeding upwards in five steps as well as five steps downwards we measure the concentration and sample size distributions in order to see their dependency on the different flow and temperature parameters.

Unfortunately the temperature sensor for the cooling temperature broke halfway through measuring the cooler flow. And due to a very long delivery time of spare parts on a relatively short time frame it was decided that the last series of the oven flow as well the last half of the cooler flow series were to be omitted from the project.

Because of the problem with our sensor there are not enough data points to do a linear regression analysis for the flow rate series of the cooler flow. Therefore the only regression analysis done are for the temperature series of the oven and cooler temperature.

14

3.8.1 Temperature Series of the Cooler Temperature T_C

For this series we look at concentration levels and size distribution for some temperatures between 11 ^{o}C and 21 ^{o}C. The temperature is raised one degree at a time and held for 40-50 minutes.

3.8.2 Temperature Series of the Oven Temperature T_H

In this series we look at concentration levels and size distribution for some temperatures between 115 ^{o}C and 135 ^{o}C. The temperature is raised two degrees at a time and held for 40-50 minutes.

3.8.3 Flow Rate Series of the Cooler Flow Q_C

The cooler flow rate series include 4 different flows between 1.00 lpm and 1.20 lpm. The flow was increased in increments of 0.05 lpm at a time and held for 40-50 minutes.

4 Results

4.1 Source Material Consumption

In Table 3 the source material consumption and the duration are shown for all runs except for the measurement series for the oven/cooler temperature and flow. Table 3 is presented as a graph with a linear regression as in Figure 5. The so called standard set of parameters was used for all experimental runs seen in Table 3, namely Q_{hot} = 0.05 lpm, Q_{cool} = 1.20 lpm, T_{hot} = 125 °C & T_{cool} = 16 °C.

Table 3: Rate of consumption.

Experiment	Δm	t	Rate
	(mg)	(h)	(mg/h)
2017-09-01	2.38	3.45	0.69
2017-09-04	3.34	6.18	0.54
2017-09-11	1.74	3.10	0.56
2017-09-25	2.71	4.08	0.66
2017-09-26/27	9.63	22.9	0.42
2017-10-03	2.54	5.40	0.47
2017-10-11	2.10	2.92	0.72
2017-10-12	4.06	4.90	0.82
2017-10-18	3.49	6.60	0.53
2017-10-19	9.03	6.51	1.38
2017-11-02	3.25	13.0	0.25
2019-07-03/04	6.11	19.6	0.31
2019-07-04/05	13.7	22.4	0.61
2019-07-08/09	4.67	13.7	0.34
Average	**4.91**	**9.62**	**0.59**
Standard Dev.	**3.39**	**7.04**	**0.27**
Minimum	**1.74**	**2.92**	**0.25**
Maximum	**13.7**	**22.9**	**1.38**

In Figure 5 the linear regression, which is forced through origo has a rather high variability that is most likely explained by the relative distance to the data point situated at Δm = 9.03 mg and t = 6.51 h.
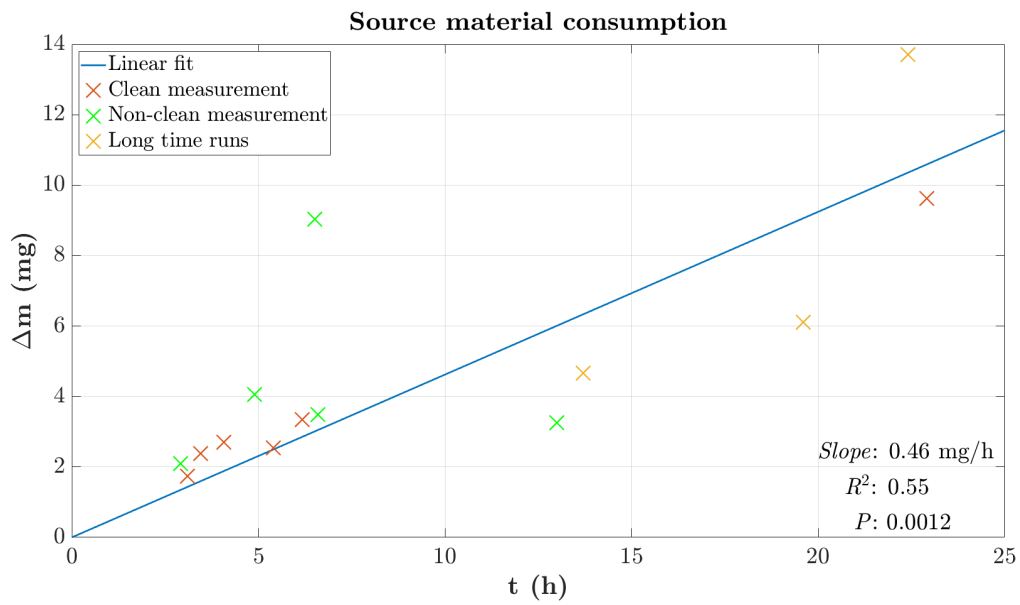
Figure 5: Source material consumption with linear regression.

4.2 Effect of Cleaning the Generator

4.2.1 Not Cleaning in Between Experiments

Figures 6 & 7 shows the number concentration over time when not cleaning in between runs. The most important to note in Figure 6 is the level jumping and how the number concentration evolve with time. In Figure 7 we see the number concentration for a long time period (22 h).
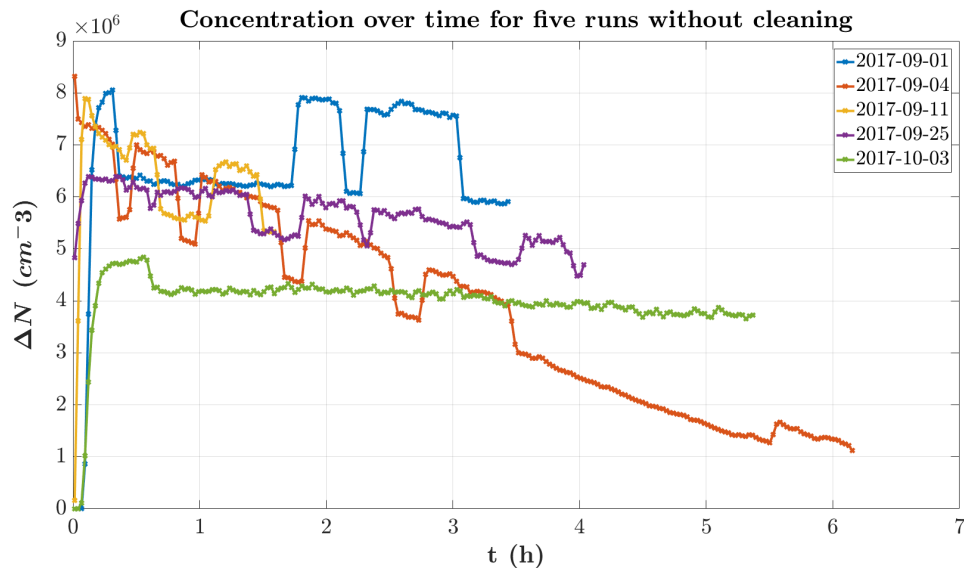
Figure 6: All but one of the experiments when not cleaning the generator in between runs. The reason the graph in Figure 7 is not included in Figure 6 is because it would compress the first five graphs with respect to the time scale as the long run is approximately six times longer than the other ones. Examples of size distributions at various times can be seen in Figure 34, 35, 36, 37 & 39 in the appendix.
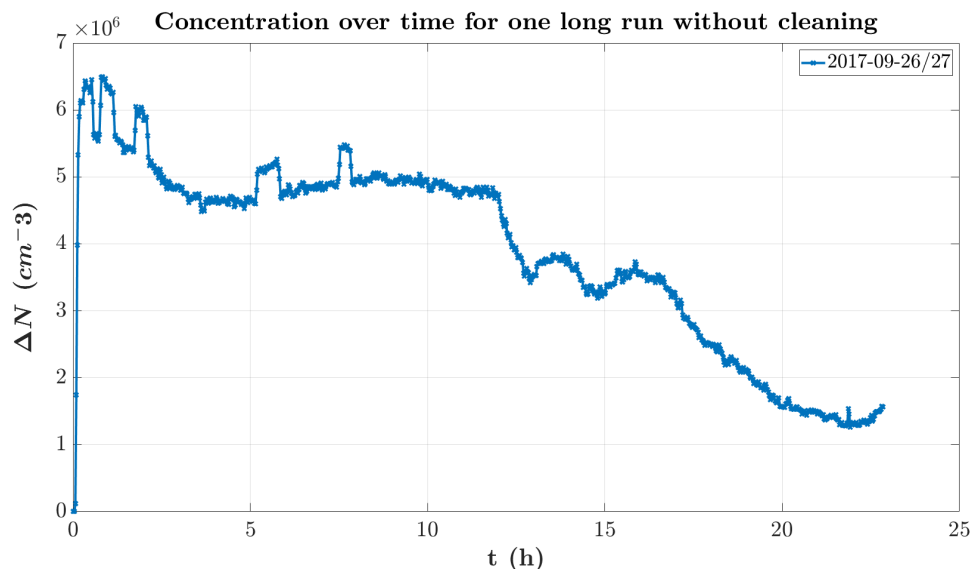
Figure 7: One of the experiments when not cleaning the generator in between runs. Examples of size distributions at various times can be seen in Figure 38 in the appendix.

18

4.2.2 Cleaning in Between Experiments

Below in Figure 8 the five runs when cleaning in between are presented with the number concentration over time. The graphs show an initial rise that is comparably lower for each session in chronological order, and except for the fourth run (2017-10-19) we see a similar rate of decrease as well as a low amount of level jumping.
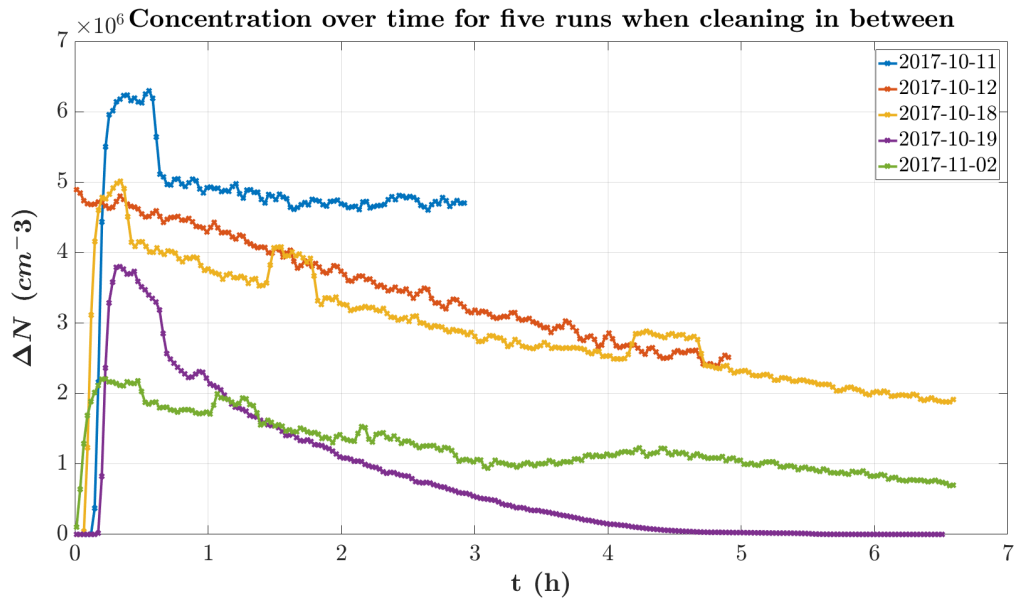
Figure 8: All of the experiments when cleaning the generator in between runs. Examples of size distributions at various times can be seen in Figure 40 41, 42, 43 & 44 in the appendix.

4.3 Reproducing Stable Concentrations Over Long Time

In Figure 9 the three long-time runs are presented as graphs showing the number concentration over time. All three experimental runs show a relatively stable concentration over long time.
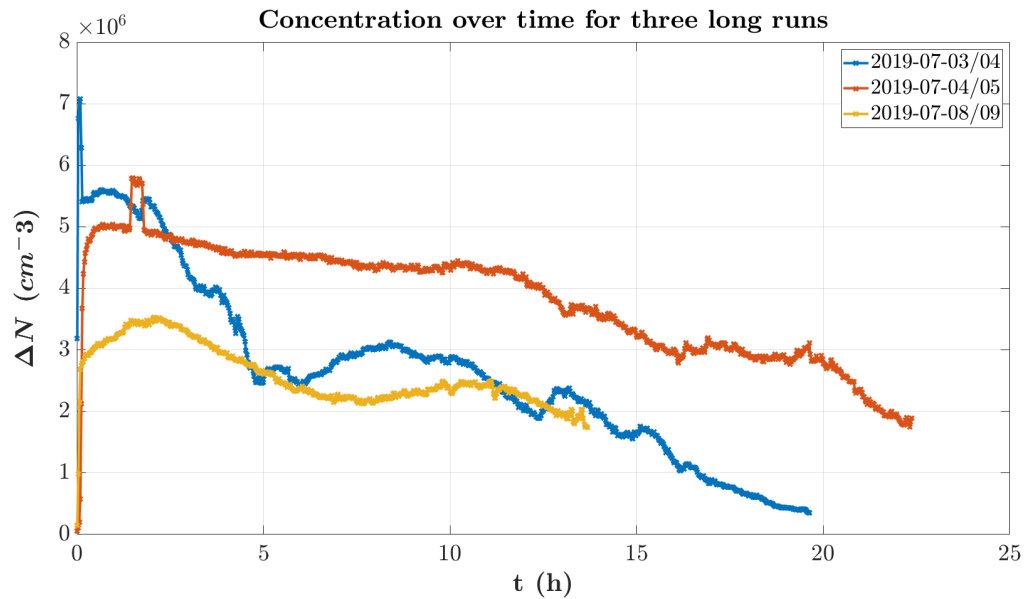
Figure 9: Trying to reproduce experiment when cleaning over long runs. Examples of size distributions at various times can be seen in Figure 45, 46 & 47 in the appendix.

4.4 Parameter Adjustment Series

The data analysis for the parameter adjustment series include observations of how the number concentration and size distributions depend on the cooling and heating temperature as well as the cooler flow. The number concentration for different cooling and heating temperatures as well as at different cooler flows, as well as the selected snapshots and their corresponding temperature or flow can be seen as circle markers on a line graph in Figure 10, 11, 19, 20 & 28.

The snapshots include information regarding the size distribution, the total number concentration, how many modes and the modal size as well as the size for the bin with the highest number concentration for different parameter settings. The size distribution with their fitted multimodal function are viewed in Figure 13, 14, 15, 16, 22, 23, 24, 25, 30 & 31.

The number concentration, the size bin with the highest concentration d_{max} and the first and second mode d_{g1} and d_{g2} are presented in a regression analysis with respect to the adjusted temperature in Figure 12, 17, 18, 21, 26 & 27. The same type of information but without the regression analysis is also found for the adjusted cooler flow in Figure 29, 32 & 33.

4.4.1 Temperature Series of the Cooler Temperature T_C

In this subsection all analysis regarding the cooler temperature are presented. It includes graphs depicting concentration over time in Figure 10 & 11. Three linear regression fits, one for number concentration in Figure 12, one for the size bin with the highest number concentration in Figure 17 and one for the fitted geometric mean sizes for the first two modes in Figure 18. As well as eight snapshots of the size distributions with their fitted multimodal distribution functions in Figure 13, 14, 15 & 16.

We see that for all the temperature intervals in Figure 10 we reach a stable concentration after a small transient in some cases. It also shows how the number concentration is lowering when increasing the cooler temperature.
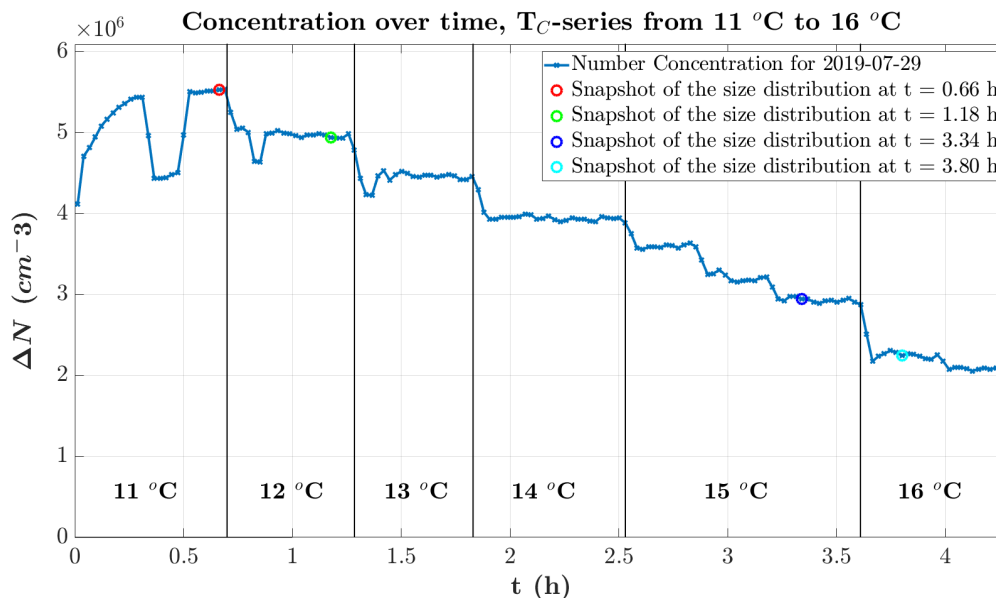
Figure 10: First half of the concentration over time with cooling temperature intervals indicated. The four snapshots of the size distribution can be seen in Figure 13 & 14.

21

The temperature intervals in Figure 11 show that we reach a stable concentration after a small transient in some cases as well as a continued inverse proportionality between the number concentration and cooler temperature.

Figure 11: Second half of the concentration over time with cooling temperature intervals indicated. The four snapshots of the size distribution can be seen in Figure 15 & 16.

The inverse proportionality is easily seen in Figure 12, which shows two concatenated experimental runs when changing the cooler temperature.
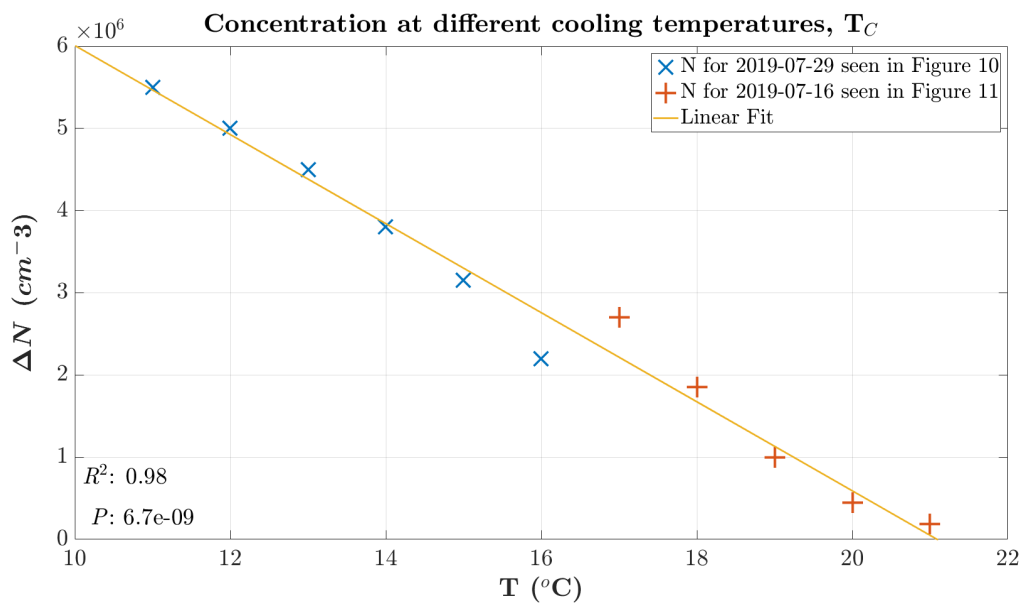
Figure 12: Concentration over cooling temperature with linear regression.

In Figure 13 & 14 there is a small increase in the size of the bin with the highest number concentration as well as the geometric mean diameter of the first and second mode when the cooler temperature is raising.

Figure 13: Snapshots of size distributions and their fitted multimodal distribution function taken at a cooling temperature of 11 °C and 12 °C.

Figure 14: Snapshots of size distributions and their fitted multimodal distribution function taken at a cooling temperature of 15 °C and 16 °C.

In Figure 15 & 16 there is a negligible increase in both the size of the bins with the highest concentration as well as more or less stationary first and second mode when the cooler temperature is raising.

Figure 15: Snapshots of size distributions and their fitted multimodal distribution function taken at a cooling temperature of 17 °C and 18 °C.

Figure 16: Snapshots of size distributions and their fitted multimodal distribution function taken at a cooling temperature of 20 °C and 21 °C.

In Figure 17 the direct proportionality between the size of the bin with the highest number concentration and the cooler temperature is easily seen.
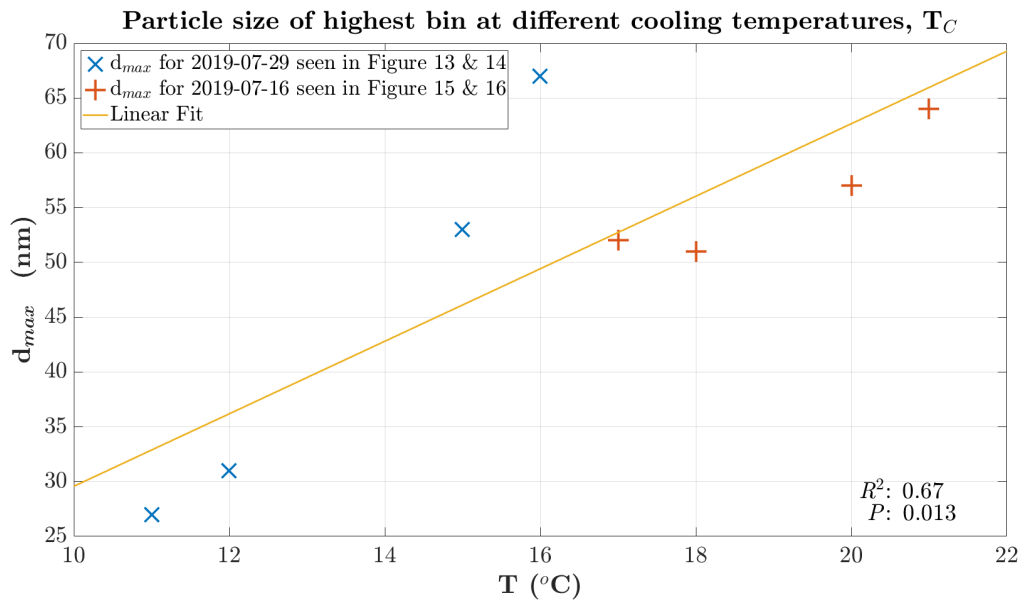
Figure 17: Particle size bin with highest concentration over cooling temperature with linear regression.

In Figure 18 the direct proportionality between the first and the second mode with respect to the cooler temperature are seen.
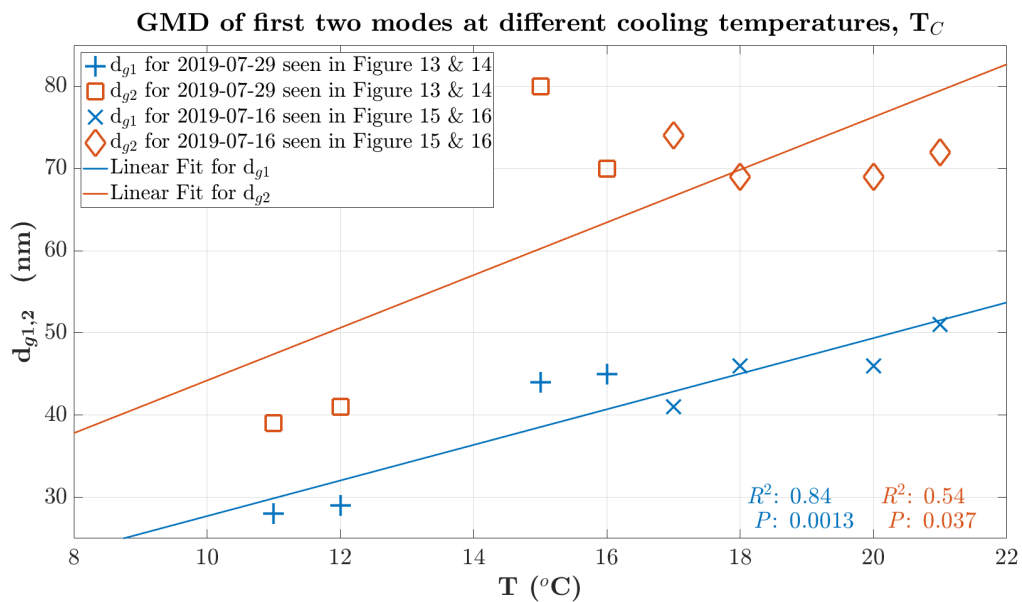
Figure 18: Fitted geometric mean particle size over cooling temperature with linear regressions.

4.4.2 Temperature Series of the Oven Temperature $\mathbf{T}_H$

In this subsection all analysis regarding the oven heating temperature are presented. It includes graphs depicting concentration over time in Figure 19 & 20. Three linear regression fits, one for number concentration in Figure 21, one for the size bin with the highest number concentration in Figure 26 and one for the fitted geometric mean sizes for the first two modes in Figure 27. As well as eight snapshots of the size distributions with their fitted multimodal distribution functions in Figure 22, 23, 24 & 25.

We see that for all the temperature intervals in Figure 19 we reach a stable concentration after a small transient in some cases. It also shows how the number concentration is raising when increasing the heating temperature.
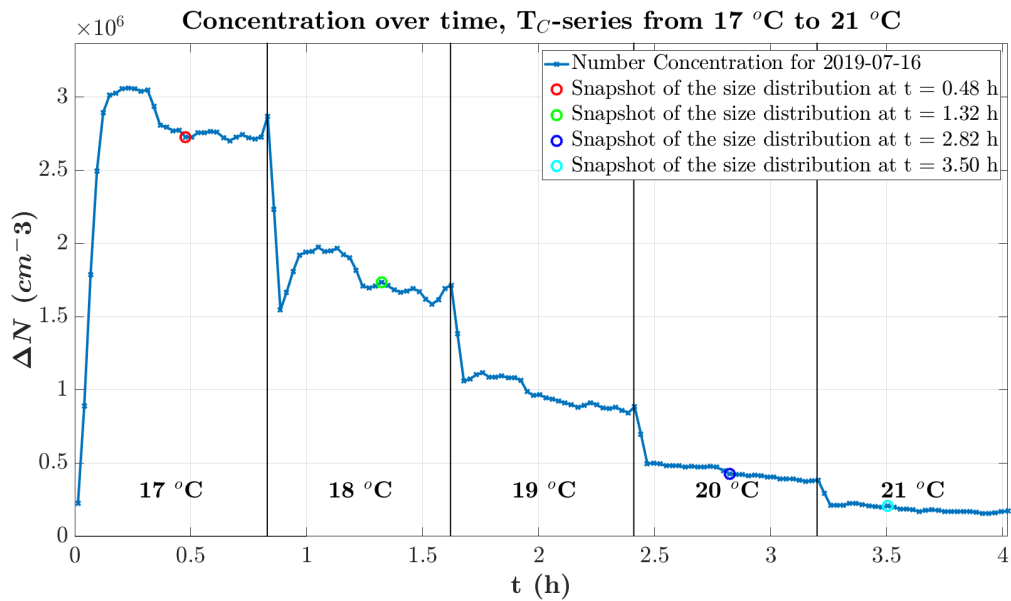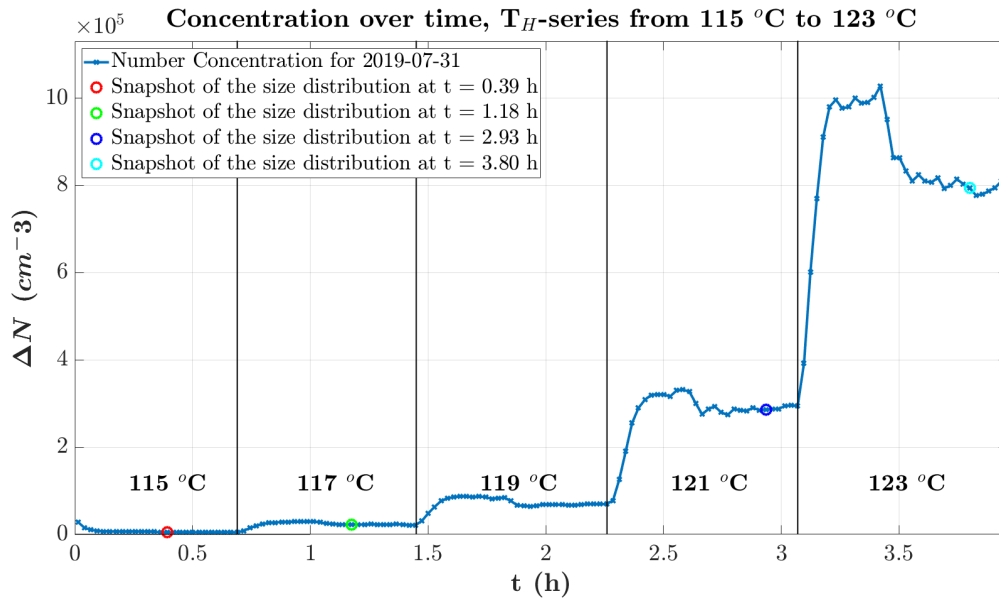

Figure 19: First half of the concentration over time with heating temperature intervals indicated. The four snapshots of the size distribution can be seen in Figure 22 & 23.

We see that for all the temperature intervals in Figure 20 we reach a stable concentration after a small transient in some cases. It also shows how the number concentration is raising when increasing the heating temperature.
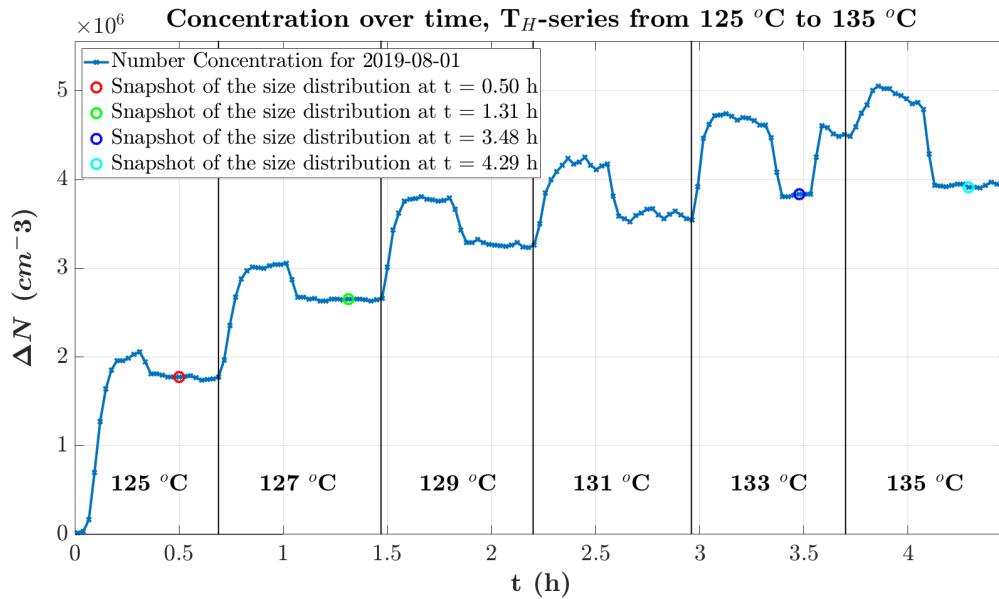
Figure 20: Second half of the concentration over time with heating temperature intervals indicated. The four snapshots of the size distribution can be seen in Figure 24 & 25.

In Figure 21, which shows two concatenated experimental runs when changing the heating temperature there is a proportionality between the heating temperature and the number concentration. There seems to be a heating temperature interval between 121 °C and 133 °C, which is more linear than the rest of the data points.
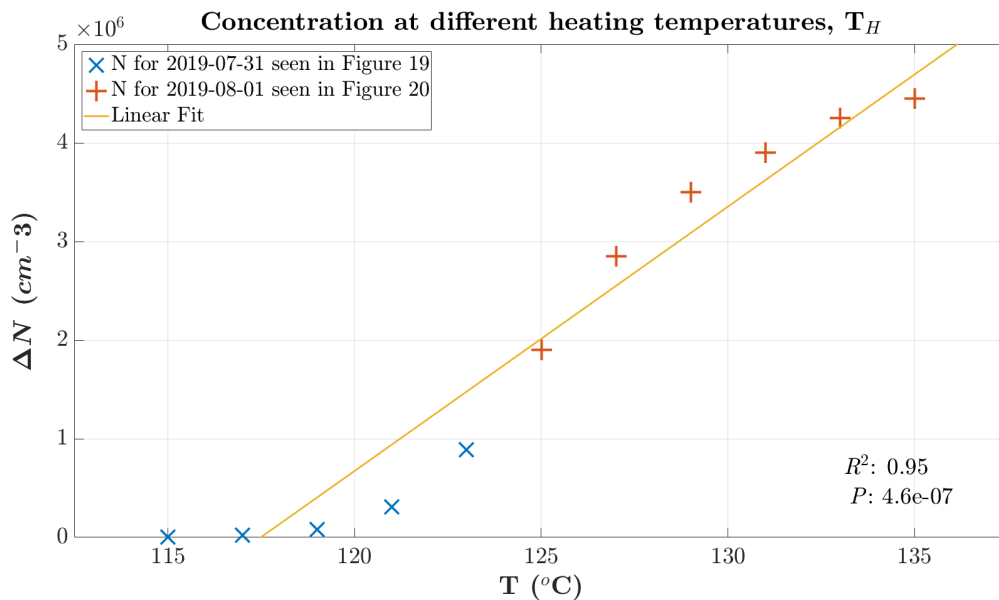
Figure 21: Concentration over heating temperature with linear regression.

27

In Figure 22 & 23 there is an increase in the size of the bin with the highest number concentration as well as the geometric mean diameter of the first mode and second when the heating temperature is raising. This is notably not the case for when the heating temperature is raised to 123 °C.
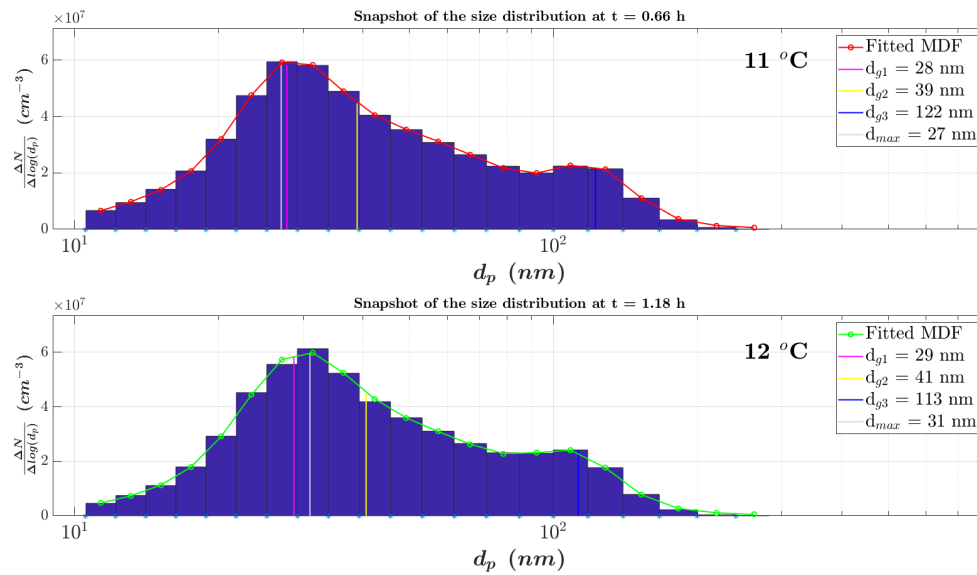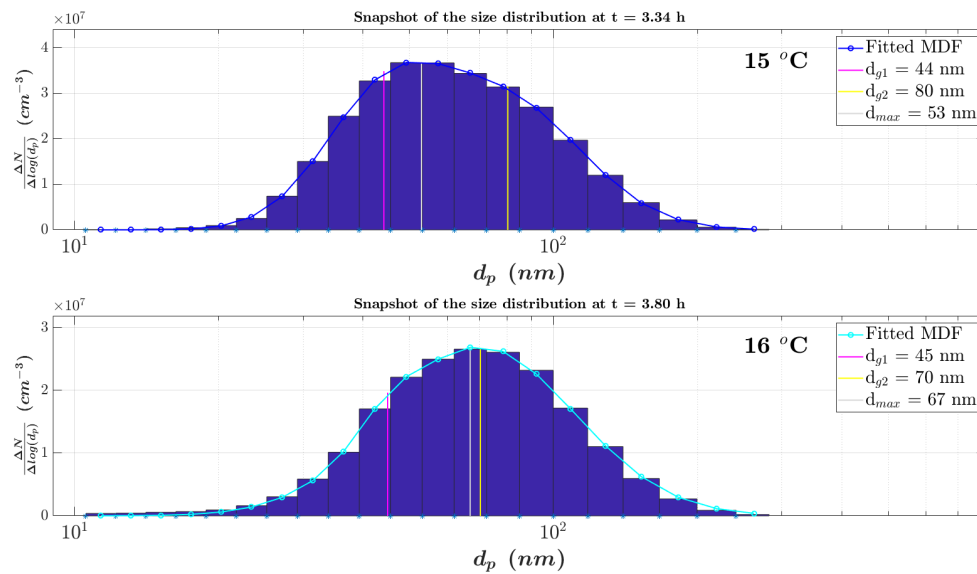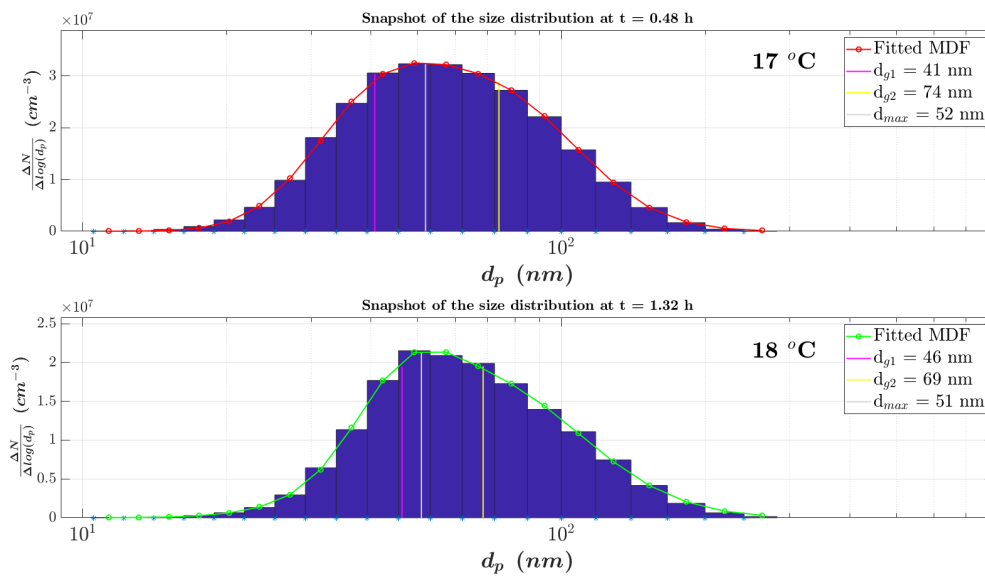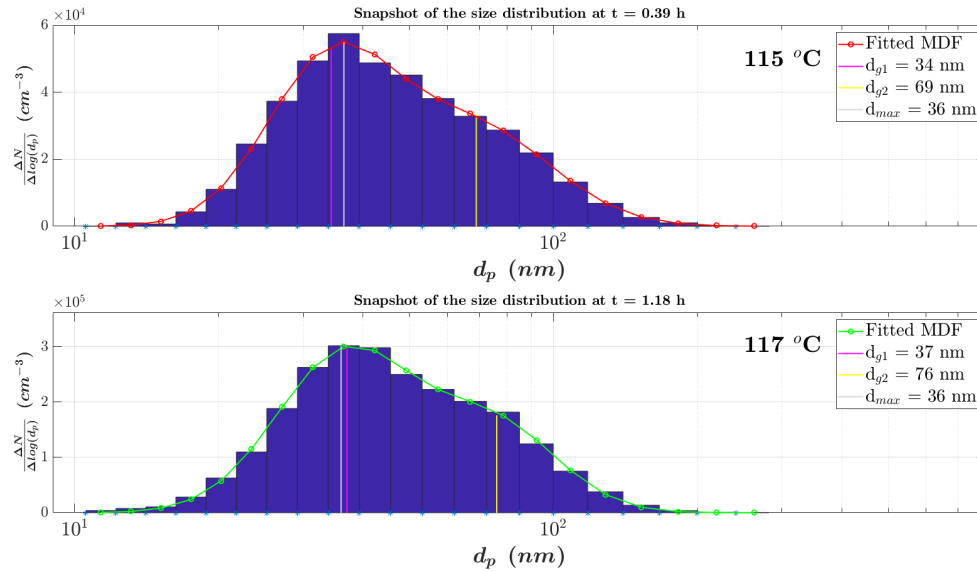

Figure 22: Snapshots of size distributions and their fitted multimodal distribution function taken at a heating temperature of 115 °C and 117 °C.
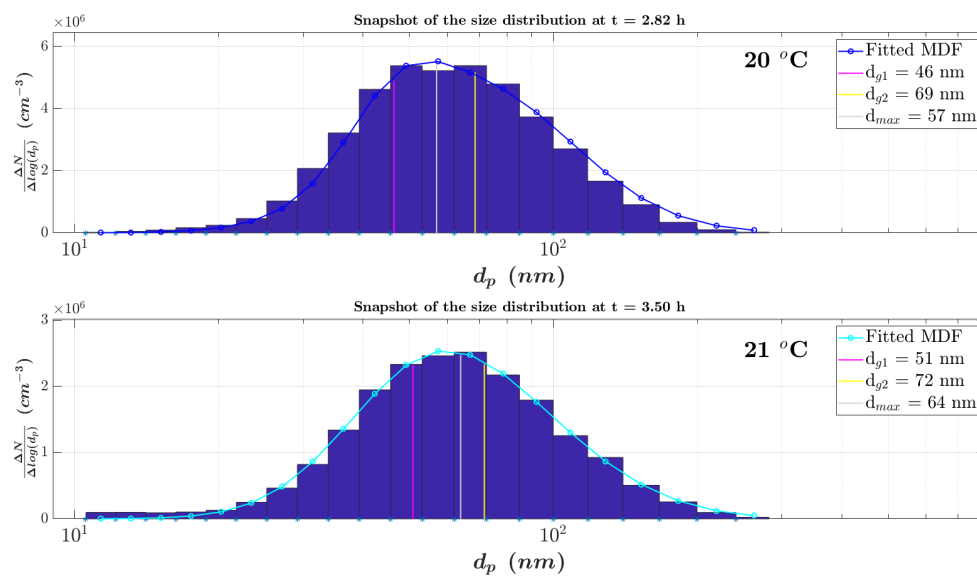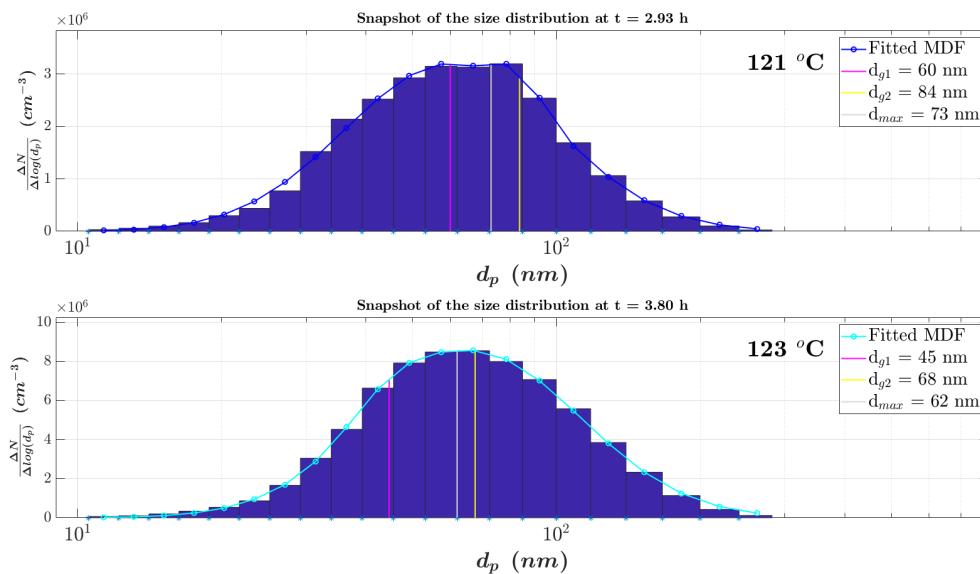

Figure 23: Snapshots of size distributions and their fitted multimodal distribution function taken at a heating temperature of 121 °C and 123 °C.

In Figure 24 & 25 there seems to be an inverse proportionality between the size of the bin with the highest number concentration and the heating temperature, that is in contrast with the previous two figures. This is also true for the first and second mode when increasing the heating temperature.
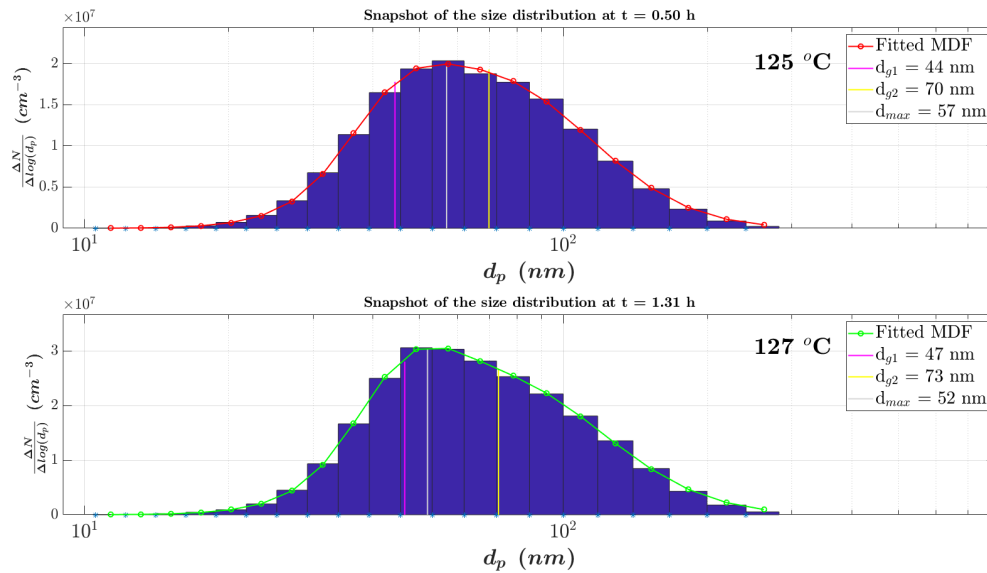
Figure 24: Snapshots of size distributions and their fitted multimodal distribution function taken at a heating temperature of 125 °C and 127 °C.
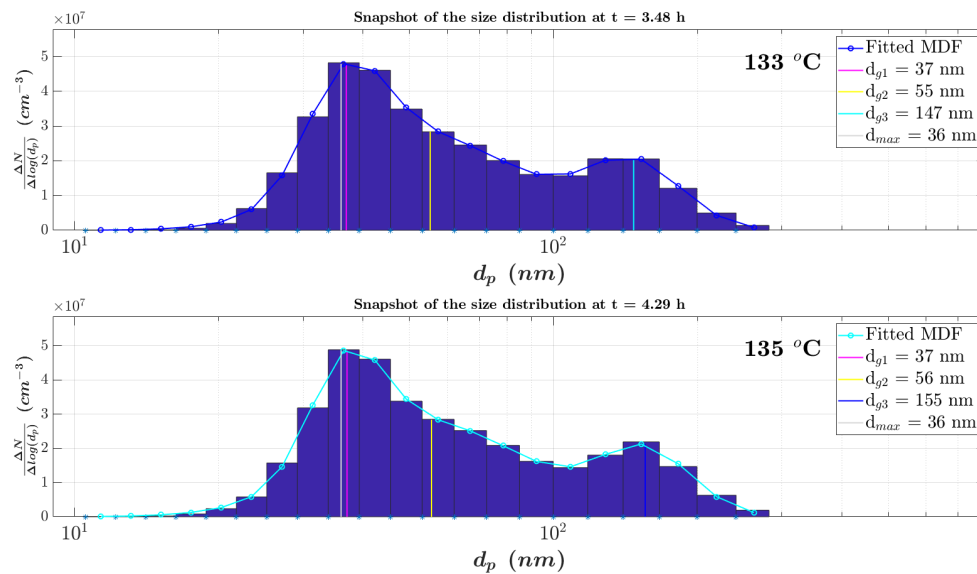
Figure 25: Snapshots of size distributions and their fitted multimodal distribution function taken at a heating temperature of 133 °C and 135 °C.

In Figure 26 the correlation between heating temperature and the size of the bin with the highest number concentration is weak. But once again as said for Figure 21, we do seem to have an interval of linearity between 121 °C and 133 °C.
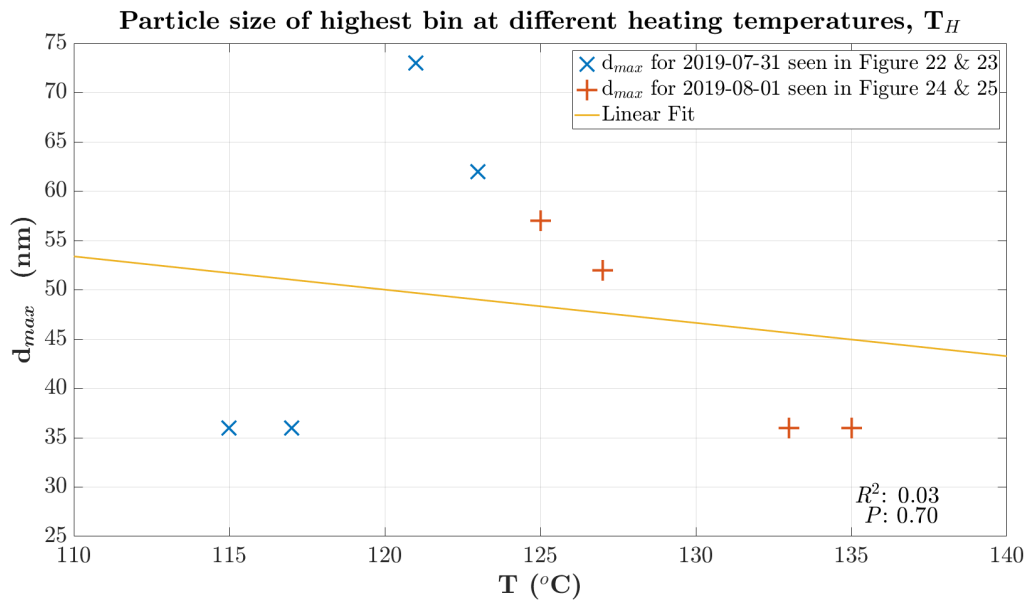
Figure 26: Particle size bin with highest concentration over heating temperature with linear regression.

In Figure 27 only the geometric mean diameter of the second mode seems to show any correlation to the heating temperature as it is lowering in size when increasing the heating temperature.
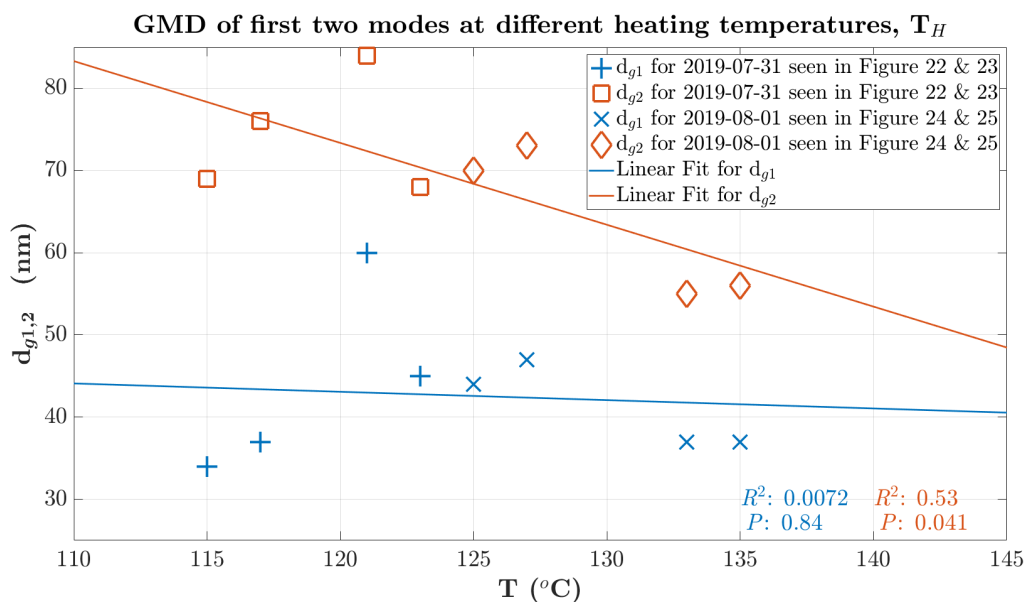
Figure 27: Fitted geometric mean particle size over heating temperature with linear regressions.

4.4.3   Flow Rate Series of the Cooler Flow $\mathbf{Q}_C$

In this subsection all analysis regarding the cooler flow are presented. It includes graphs depicting concentration over time in Figure 28. Three data sets for cooler flow dependency, one for number concentration in Figure 29, one for the size bin with the highest number concentration in Figure 32 and one for the fitted geometric mean sizes for the first two modes in Figure 33. As well as four snapshots of the size distributions with their fitted multimodal distribution functions in Figure 30 & 31.

We see that for all the flow intervals in Figure 28 except for when Q_C=1.00 lpm a stable concentration is reached. This is more easily readable when the number concentration is plotted with respect to the discrete cooler flow values as seen in Figure 29.
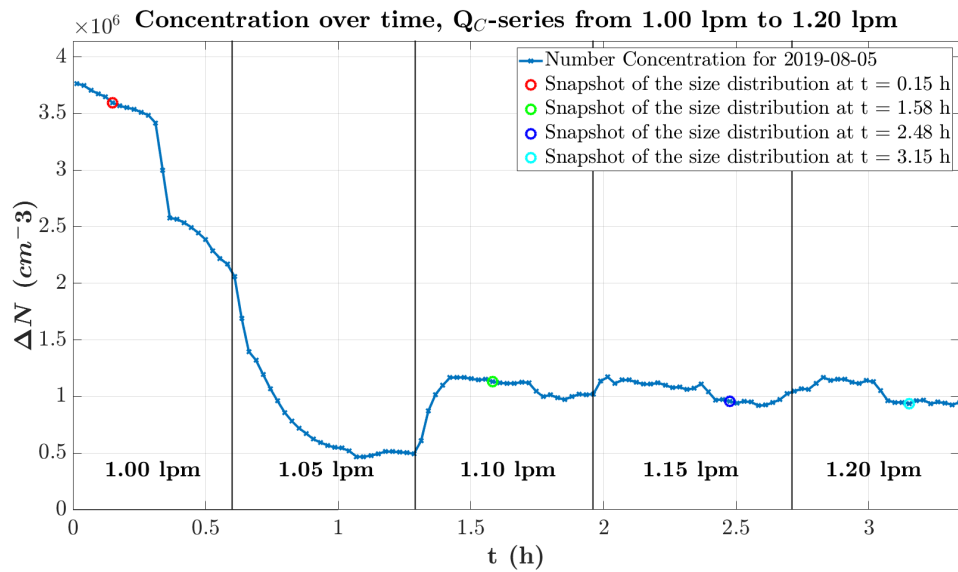
Figure 28: The concentration over time with cooler flow intervals indicated. The four snapshots of the size distribution can be seen in Figure 30 & 31.
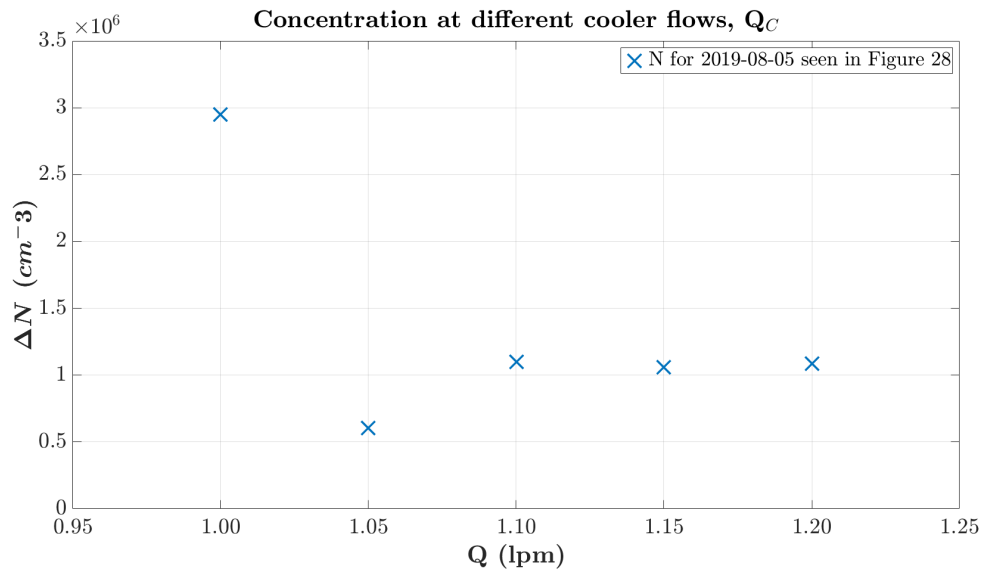
Figure 29: Concentration over cooler flow.

In Figure 30 & 31 there is an increase in the size of the bin with the highest number concentration for the first three cooler flows, which is also the case for the geometric mean diameter of the second mode. There is also a first occurrence of a completely (according to the data fitting) mono-modal size distribution for the last cooler flow at 1.20 lpm.
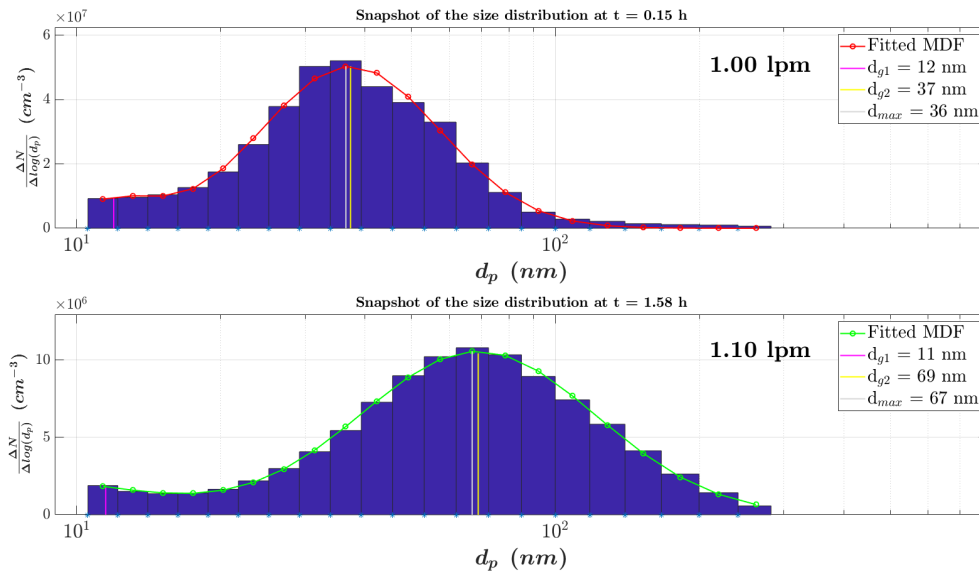
Figure 30: Snapshots of size distributions and their fitted multimodal distribution function taken at a cooler flow of 1.00 lpm and 1.10 lpm.
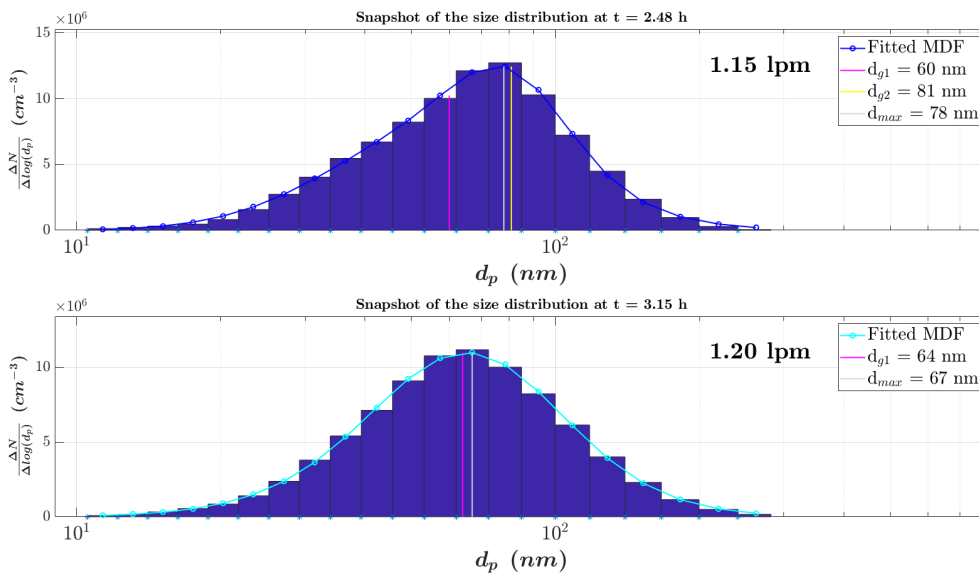
Figure 31: Snapshots of size distributions and their fitted multimodal distribution function taken at a cooler flow of 1.15 lpm and 1.20 lpm.

Figure 32 & 33 shows that there generally seem to be an increase in the size of the bin with the highest number concentration as well as the geometric mean diameter of the first and second mode.

Particle size of highest bin at different cooler flows, Q_C
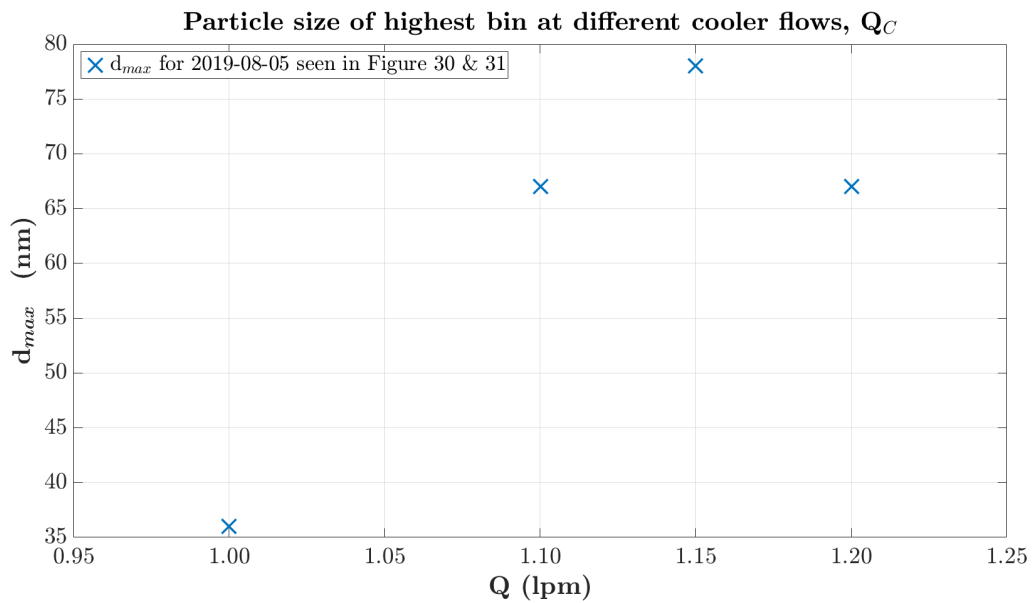
Figure 32: Particle size bin with highest concentration over cooler flow.

GMD of first two modes at different cooler flows, Q_C
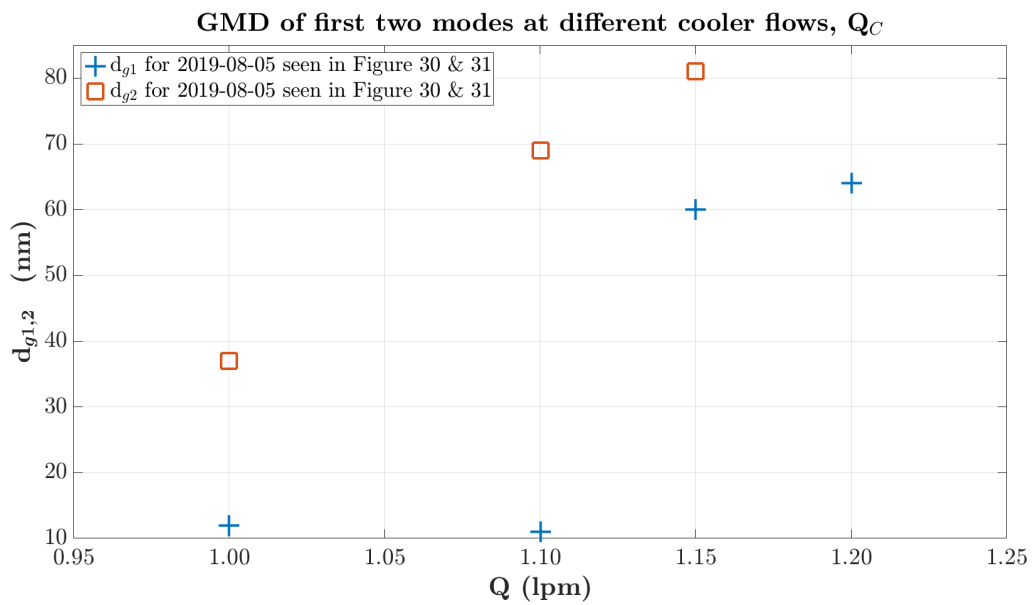
Figure 33: Fitted geometric mean particle size over cooler flow.

5 Discussion

The results of the project show the source material consumption, the effects of cleaning the generator as well as how the aerosol size distribution and number concentration depend on three of the four different adjustable parameters.

Trying to fit this project in the context of current relevant research has been hard. Most of the articles regarding nanoparticle generation cover metallic nanoparticles and different types of nanotoxicology such as for large scale manufacturing of semiconductor particles, [25] and inhalation toxicity studies. [26] [27] Others have successfully made particle generators with the goal of producing radioactive aerosols for lung scintigraphy. These typically generate particles within the range of 250 to 600 nm. [28]

One reoccurring problem with the generator studied in this thesis is that it produces quite a lot of particles in the 100-200 nm range, given that we are interested in producing a monodisperse aerosol centered around 50 nm without particles larger than 100 nm. This is most likely the result of coagulation depending on too high concentrations or too much turbulence, decreasing the concentration is easily done by raising the cooler temperature or by lowering the heating temperature. The correlations of number concentration and the temperatures are clearly understood and confirmed within this project as discussed in Section 5.4.1 & 5.4.2. In theory the turbulence could be lowered by increasing the flow parameters so that the flow is more laminar.

5.1 Source Material Consumption

The consumption of source material is very low at about 0.59 ± 0.27 mg/h. and does seem to fit linearly with the duration of an experiment. This is positive as a stable consumption indicates that the generator easily can be used for many hours at a time without the need to refill.

A linear regression was made out of the two variables Δm and t as shown in Figure 5. We have a R-squared value at 0.55 that is acceptable. The linear regression strongly suggests that we have reached statistically significance due to the low p-value of 0.0012.

The major contributor to the variability in the data seems to be one run that experienced a much higher relative deviation in source material consumption in comparison to the rest of the runs seen in Figure 5. The non-clean run corresponding to the data point at $\Delta m = 9.03$ mg, which had a duration of 6.51 h. This run can be seen in Figure 43 (Appendix) and is an outlier with regards to an exponentially decreasing number concentration. However the exponential decrease in the number concentration might be due to an issue of low butanol in the CPC and if so would not impact the rate of consumption.

It is interesting to note that the average value of the rate of consumption is equal to 0.59 mg/h while the slope of the linear fit seen in Figure 5 gives a value of 0.46 mg/h. If more experiments were to be made, we may see the average of consumption rate getting closer to the slope of the regression line. This leads to the conclusion that the actual rate of consumption should lie somewhere in between the two values.

5.2 Effect of Cleaning the Generator

The main effect of cleaning the generator is that we see a reduction in the frequency as well as the magnitude of level jumping with regards to the number concentration. There also seems to

be a more reproduceable behavior when the generator is cleaned in between runs. Almost all of these runs in Figure 8 do show similarity with respect to the the rate of decrease in number concentration compared to the non-cleaned experimental runs shown in Figure 6.

5.2.1 Not Cleaning in Between Experiments

There seem to be a trend going from a rather wide distribution to a more narrow one over time when looking at the snapshots of the runs in Figure 34, 35, 36, 37, 38 & 39 (Appendix) in chronological order. The first four runs totaled almost 17 hours and looked similar to each other compared to the last two runs that totaled about 28 hours. The first four shorter experimental runs all had a relatively wide distribution, which alternated between bi- and tri-modal. Their major peak was situated at relatively low particle sizes in the range of 26 to 42 nm. The last two runs seem almost monodisperse and whose major peak is situated at 50 to 60 nm.

Looking at Figure 6 one of the first things you see is the variation in concentration within a single experiment. E.g. for the first experiment (2017-09-01) the concentration reaches heights of $8 \cdot 10^6$ cm^{-3} after the initial rise and then suddenly falls of to about $6.2 \cdot 10^6$ cm^{-3}. After a stable period of about 1.4 h there is a sudden rise of concentration to a similar level that we observed after the initial rise. The fall to the lower concentration level and another raise of the level seems to be between two fixed values. One initial assumption that could be made is that we are dealing with a build up of material in the nozzle of the oven when the material first come in contact with the cooling part of the generator. Then acting as a plug that after a while releases and leads to a sudden burst increase of the concentration until another plug builds up and therefore decreases the concentration.

However, I would think that if we are dealing with a build-up, that effectively strangles the throughput of particles, we should see a gradual decrease and increase of the volume. Not the sudden change that is seen in the graph.

This phenomena is observed in all of the graphs in Figure 6, however the one run (2017-10-03) which shows the lowest frequency of "level jumping" is the one that was made last in chronological order. This could be an important observation as the last run also represents the generator in its least clean state.

To continue finding a pattern in the data there also seems to be a reduction in the size of the "level jump" when looking at the graphs in chronological order. Assuming that the phenomena is in fact a result of the 'build up and release'-hypothesis the more material hindering the flow, the less the impact (smaller level jumps) of release would be, given that we already have a baseline level of compound A in the solid phase that does not release when layers upon layers have been let to grow.

What also is interesting to note is that the second (2017-09-04) and third (2017-09-11) run decreases continually over time. While at least the first (2017-09-01) and the last (2017-10-03) run seems to be reducing at a much slower pace.

The long time run seen in Figure 7 shows an interesting point at about the 4-5 hour mark where the gradual decrease in concentration seems to be at an end, followed by a low increase in concentration for about 5-6 hours before hitting a sharp fall in concentration at the 12-hour mark. This could be a result of how coagulation decreases the number concentration by making multiple particles into fewer, then when the concentration is low enough that the probability of coagulation decreases (as it is proportional to the number concentration squared) we see an increase in particles once more.

In the third run (2017-09-11) an almost clear cut bi-modal distribution is seen in Figure 36 (Appendix), especially in the second snapshot. The major peak of the first mode in the first and second snapshot are centered at 32 and 38 nm, respectively, while the second mode of the first and second snapshot are 103 and 89 nm, respectively. The mode centered on 103 nm is most likely a coagulation mode and I would suspect that the mode centered on 89 nm is as well, however it is close to the lower limit of what I would consider to be an almost pure coagulation mode. This reasoning stems from the theory around how coagulation modes often appear at almost a magnitude larger than the size of the primary particles, which can be seen schematically in Figure 3. [17]

Looking at the snapshots of the size distributions in the long time run (2017-09-25/26) shown in Figure 38 (Appendix) both snapshots are taken almost 10 hours apart and still look quite alike each other. In contrast to the earlier runs seen in the figures in the same section of the appendix, the distribution seems to be quite narrow with one major peak at 55 and 60 nm for the first and second snapshot, respectively. The major peaks consists of two modes located at 46 and 79 nm for the first snapshot while we see the two modes of the second snapshot located at 50 and 69 nm. Even though we don't see a clear pure coagulation mode for either of the snapshots we still see a tail of the distribution lingering over the 100-120 nm range, so there still seems to be some large particle coagulation going on.

5.2.2 Cleaning in Between Experiments

The first thing to notice when comparing the experiments which were cleaned in between runs in Figure 8 with the non-cleaned runs in Figure 6 & 7 is that there seem to be a smaller amount of level jumping, which is discussed in Section 5.2.1. This could reinforce the hypothesis that there in fact are plugs, which are more easily generated when not cleaning due to layers of solid phase source material in the oven's nozzle close to the cooling compartment.

One would expect the initial levels of concentration to be about the same for the different runs, however it could be smaller from one run to the next due to a lessening amount of source material. This could be easily checked by adding an amount of source material equaling the amount consumed in the previous run.

Once again looking at Figure 8 the first run (2017-10-11) seems to be the most stable one and all others except the fourth (2017-10-19) shows a gradual decrease in number concentration. The number concentration in the fourth run is so vastly different that I suspect that it is related to a butanol deficiency in the CPC that wasn't noted in my experimental diary.

The size distribution for the chronologically first of the graphs in Figure 8 (2017-10-11) can be seen in Figure 40 (Appendix) and shows a relatively wide distribution that almost resembles a bi-modal distribution. The major peak is situated at 44 and 45 nm for the first and second snapshot, respectively, as well as a secondary mode situated at 84 and 83 nm in the first and second snapshot, respectively. If my reasoning in Section 5.2.1 regarding that the lower limit of the mode pure coagulated particles is located at about 90 nm this run represents the mode with the highest geometric mean diameter of non-coagulated particles at 84 and 83 nm. This naturally comes with a "coagulation tail".

When looking at the the first run in Figure 40 (Appendix) the concentration is approximately equal at the two snapshots at 0.72 h and 2.68 h and the size distribution of the two snapshots also look close to identical. Looking at the second run as seen in Figure 41 (Appendix), the two snapshots taken at 0.64 h and 2.68 h, are taken with almost the same amount of time elapsed as for the first run, and also show that there is close to no change in the size distributions.

Between these two experiments the only differing outcome is that the number concentration is lower for the second snapshot in the second run, which shows a good case for reproducibility.

5.3 Reproducing Stable Concentrations Over Long Time

The first long time run (2019-07-03/04) seen in Figure 9 shows a rather interesting behaviour. After a solid decrease in concentration for about five hours the concentration started to rise again. This could possibly be due to a shift in particle diameters towards smaller particles, but it could also be due to a buildup of material that is released as per the 'build up and release'-hypothesis.

What seems to show great promise of reproducibility is the fact that according to the size distributions in Figure 45, 46 & 47 (Appendix) the first snapshot of each run has a clear trend moving from a more or less bi-modal distribution towards a much more narrow one. As seen in Figure 45 (Appendix) the first snapshot of the first run (2019-07-03/04) has a major peak at 32 nm consisting of two modes situated at 28 and 50 nm as well as an almost pure coagulation mode at 121 nm. This looks very much like the size distribution of the first snapshot seen in Figure 46 (Appendix)in the second run (2019-07-04/05) whose major peak at 38 nm consists of two modes at 34 and 53 nm as well as an almost pure coagulation mode at 122 nm. Comparing these two snapshots to the first snapshot of the third run (2019-07-08/09) seen in Figure 47 (Appendix) there are some clear similarities such as a bi-modal distribution with the exception of having an overall more narrow distribution bringing the coagulation mode and major peak closer to each other. With that said the major peak is situated at 44 nm and the coagulation peak is found at 101 nm, the difference in size between the major peak and coagulation mode goes from about 80-90 nm to about 60 nm.

The major similarity that connects to the coagulation mode between the first two runs in contrast to the third run is the number concentration at the time of the first snapshot. The first two runs have a number concentrations of about 5-6 $\cdot 10^6$ cm^{-3} compared to the value of the third run, which is about half that number, and the amount of coagulation that occurs is proportional to the number concentration as the likeliness of collision between two particles are that much greater when there is less space to move freely.

Moving on to the second snapshot of the three runs we see that in each of the runs the major peak in the size distribution shifts towards higher sizes when comparing to the place of the major peak in the respective three first snapshots, in the first run we move from 32 nm to a major peak at 42 nm consisting of two modes situated at 39 and 66 nm. In the second run we move from 38 nm to a major peak at 52 nm and in the third run the major peak moves from 44 nm to 58 nm consisting of two modes at 49 nm and 73 nm.

5.4 Parameter Adjustment Series

For the three different measurement series where the cooling temperature, heating temperature and the cooler flow were adjusted in steps. We observed clear trends in the heating temperature and the cooling temperature explainable by theory. In contrast to when observing an increase in particle size when increasing the cooler flow, which is unexpected. [29]

5.4.1 Temperature Series of the Cooler Temperature T_C

The general trends for the series that are seen in Figure 10 & 11, by looking at the regression fits in Figure 12, 17 & 18 are that when the cooling temperature increases the number concentration goes down, while at the same time the amount of larger particles increases as well

as their sizes compared to lower cooling temperatures. These results are also found for e.g. evaporation/condensation metal nanoparticle generation. [30]

It is clear that there is a inverse proportionality between the number concentration and the cooling temperature T_C. This is shown in Figure 12 where the linear fit has a very high R-squared value at 0.98 and very low p-value at $6.7 \cdot 10^{-9}$, i.e. the model explains the variation very well and the data is significant. This could be explained by the fact that a low cooling temperature forces a rather fast nucleation and condensation of the aerosolized compound A unlike at higher temperatures where the nucleation and condensation undergoes at a much slower pace.

The size distributions in Figure 13 shows that we have almost pure coagulation modes at 122 nm and 113 nm at 11 °C and 12 °C, respectively. This is a consequence of the relatively high number concentration. Seeing how the number concentration decreases with temperature, we fail to find any other almost pure coagulation modes for when the cooler temperature is 15 °C, 16 °C, 17 °C, 18 °C, 20 °C or 21 °C. This is expected behaviour considering that the number concentration is going down.

When looking at Figure 17, we see that the size-bin with the highest concentration d_{max} increases with temperature. The regression fit has a reasonably well R-squared value at 0.67 as well as a very good p-value at 0.013 that indicates that our model fits with the data. Combining that fact with the results presented in Figure 18, we see that increasing particle sizes seems to correlate with a higher cooling temperature. The R-squared value at 0.84 and a p-value of 0.0013 for the first mode seem to indicate that the particle size have a high likelihood of correlating with cooling temperature. Although that the linear regression for the second mode with respect to the cooling temperature does not hold up to the same level of scrutiny based on the merely acceptable R-squared value at 0.54 and the p-value at 0.037, the probability of a correlation seems to be there for a low enough confidence interval.

5.4.2   Temperature Series of the Oven Temperature T_H

As one might suspect there is a direct proportionality between the heating temperature T_H and the concentration. This is clearly shown in Figure 21. The R-squared value at 0.95 and p-value at $4.6 \cdot 10^{-7}$ are very good, however looking at the graph it does seem like there is chance that the fit should not be linear. If one would do more measurements for even higher temperature and the pattern would follow the immediate trend it almost looks like the concentration would plateau. This could be a result of a greater deal of coagulation occurring in a faster rate than new particles nucleate, as coagulation effectively lowers the number concentrations because multiple particles join each other. This is a probable hypothesis as coagulation is proportional to the number of particles squared, which is also easy to imagine as there are less and less space to move around freely for the particles. Comparing these results with other evaporation/condensation generated organic aerosols it is easy to conclude that we are looking at a general pattern with respect to the effects of changing the heating temperature. [31]

Looking at the size distributions in Figure 22, 23, 24 & 25 the main outlier of the size distributions are the ones when the heating temperature is 133 °C & 135 °C. These two size distributions shown in Figure 25 both have an almost pure coagulation mode at 147 and 155 nm, the same logic that has been used multiple times before in this document dictates that a higher number concentration leads to more coagulation. This is naturally the case for the two highest heating temperatures as this leads to the highest number concentration.

The size bin with the highest concentration d_{max} is mapped with respect to the heating tem-

peratures as shown in Figure 26, and the linear regression fit gives a poor R-squared at 0.027 and p-value at 0.70. However, if we omitted the two first data points it would seem to show a negative proportionality, but arguing that these two data points doesn't hold up as reasonable points seem difficult. This is difficult because at lower heating temperatures there may be such a low number of evaporated molecules available for nucleation and growth. An interesting observation is that the two data points for the lowest heating temperatures coincide with the two data points for the highest heating temperatures. It would be interesting to measure more data points inside the region of heating temperatures 120 °C and 130 °C to see if the seemingly clear linear relationship exists between these two points, as well as measure at more temperatures outside this region both over and under said temperatures to see if we in are observing our systems realm of operation, i.e. the temperatures that are available to us if we are interested in reproducing and controlling the particle sizes with the help of the heating temperature.

The linear regression fit of the two different modes with respect to the heating temperature in Figure 27 the first mode does not seem to show any proportionality to the heating temperature with a R-squared value at 0.0072 and a p-value at 0.84 while the second has a borderline fit with a R-squared value at 0.53 and a p-value at 0.041. It is quite interesting to see that only one of the modes seem to show any type of correlation, and if I had to guess beforehand I would guess that the second mode is the one that would show it. This is becuase of the multiple mechanisms that affect higher sized particles because of coagulation. But that guess would have been that we expect the second mode to move higher and higher in sizes due to more coagulation at higher temperature as a consequence of the denseness of particles.

5.4.3 Flow Rate Series of the Cooler Flow Q_C

Even without a regression analysis it is easy to see in Figure 29 that there does not seem to be any correlation between the number concentration and the diluting flow Q_C, although based on very few data points. However, when looking at Figure 32 the size bin with the highest concentration d_{max} seem to be a shift towards larger sizes for higher flows. This also holds true for the size of the geometric particle size modes with respect to different cooler flows as shown in Figure 33.

That an increase in the cooler flow results in larger particle sizes seems wrong based on the theory, because an increase in the flow would lessen the time particles spend in the cooling chamber where condensation occurs. As condensation is responsible for particle growth one would expect that less time spent in the cooling chamber would lead to smaller particles. But as mentioned earlier there are very few data points to make a rigorous analysis for this measurement series. [32]

6 Conclusions

This project set out to characterize a new type of nanoparticle generator by looking at some fundamental functions of it. Measuring the source material consumption, observing the ability of nanoparticle generation under different circumstances, testing it over long times and adjusting the different available parameters all fall into the category of characterization. All of the experiments together proved to give some insight into the fundamental functions of the generator and showed that for compound A it did produce a sufficiently high number concentration over long times with particles that fall into the range of 10-100 nm. It is now clear that the generator shows great promise as it does show a stable high concentration with particles that fall into the range of 10 to 200 nm.

According to the measurement series regarding the particle sizes and the number concentrations with respect to the cooler temperature T_C and the heating temperature T_H both seems to follow what is theoretically predictable. This indicates that the generator design does not hold unexpected faults in regards to the process of generating nanoparticles under the method of 'evaporation nucleation condensation'. This in turn would indicate that the generator is well on its way to completion.

Multiple experiments such as doing a measurement series for the oven flow Q_H still needs to be done in order to fully examine the type of effect each of the adjustable parameters has on the outcome of the aerosol. A natural path going forward is also trying to reproduce the measurement series for the parameter adjustments but with much higher resolution and range. E.g. instead of having just 8-11 data points for the regression analysis that number should be much higher and also extending below and above the lower and upper limit of the parameter in question.

The experimental sessions that included observing the effect of cleaning and not cleaning in between runs ended up taking a too much time of the project as a whole. Instead I would have used that time to include a much larger data set in the parameter adjustment series.

One of the difficult parts of this project has been to put it into context of current relevant research within the same area of science. This is in part due to the nature of working with a wholly new type of generator. Most of the articles about nanoparticle generation regards metallic particles, while we in this project looks at organic nanoparticles.

The next step in becoming a better version of already existing medical diagnostic tools is to try and aerozolise radioactive compounds and make sure that the generated aerosol holds the same quality with respect to stability and desired size distribution as it does for compound A. By extending the function of the generator beyond the one source material used for this project it is well on the way to be used as a medical tool for ventilation/perfusion scans. The great advantage that this generator will have is the ability to produce particles in the aforementioned range as this will lead to a full coverage of all areas of the lungs. This is due to the nanoparticles ability to deposit in the tracheobronchial and alveolar structures of the lung.

References

[1] J.H. Seinfeld and S.N. Pandis. Atmospheric chemistry and physics: From air pollution to climate change. *Wiley-Inter Science*, 1998.

[2] P. Gerde, P. Ewing, and A. Ryrfeldt. A novel method to aerosolize powder for short inhalation exposures at high concentrations: isolated rat lungs exposed to respirable diesel soot. *Inhalation Toxicology*, 16(1):45–52, 2004.

[3] J. Löndahl, W. Möller, and J. H. Pagels. Measurement techniques for respiratory tract deposition of airbrone nanoparticles a critical review. *Journal of Aerosol Medicine and Pulmonary Drug Delivery*, 27(4):229–254, 2014.

[4] A. Dowling, R. Clift, et al. *Nanoscience and nanotechnologies: opportunities and uncertainties*. The Royal Society and The Royal Academy of Engineering, 2004.

[5] Möller W. Pagels J.H. Kreyling W.G. Swietlicki E. Löndahl, J. and O. Schmid. Measurement techniques for respiratory tract deposition of airborne nanoparticles: a critical review. *Journal of aerosol medicine and pulmonary drug delivery*, 27(4):229–254, 2014.

[6] J. A. Parker, R. E. Coleman, E. Grady, H. D. Royal, B. A. Siegel, et al. Society of nuclear medicine practice guideline for lung scintigraphy 4.0. *Journal of Nuclear Medicine Technology*, 40(1):57–65, 2012.

[7] M. Bajc, J. B. Neilly, M. Miniati, C. Schuemichen, M. Meignan, and B. Jonson. Eanm guidelines for ventilation/perfusion scintigraphy. *European Journal of Nuclear Medicine and Molecular Imaging*, 36(8):1356–1370, Aug 2009.

[8] M. Messing. The advantages of spark discharge generation for manufacturing of nanoparticles with tailored properties. *Journal of Green Engineering*, 5(4):83–96, 2015.

[9] A. Jaworek and A. T. Sobczyk. Electrospraying route to nanotechnology: An overview. *Journal of Electrostatics*, 66:197–219, 2008.

[10] J. B. Harstad, M. E. Filler, W. T. Hushen, and H. M. Decker. Homogeneous bacterial aerosols produced with a spinning-disc generator. *Applied Microbiology*, 20(1):94–97, 1970.

[11] D. A. Japuntich, J. I. T. Stenhouse, and B. Y. H. Liu. Conditions for monodispersity of heterogeneous condensation aerosols using dimensionless groups. *Journal of Colloid and Interface Science*, 136(2):393–400, 1990.

[12] M. Alonso, F. J. Alguacil, M. I. Martin, Y. Kousaka, and T. Nomura. Aerosol particle size growth by simultaneous coagulation and condensation with difusion losses in laminar flow tubes. *Journal of Aerosol Science*, 30(9):1191–1999, 1998.

[13] H. V. Nguyen, K. Okuyama, T. Mimura, Y. Kousaka, R. C. Flagan, and J. H. Seinfeld. Homogeneous and heterogeneous nucleation in a laminar flow aerosol generator. *Journal of Colloid and Interface Science*, 119(2):491–504, 1987.

[14] Igor Agranovski. *Aerosols - Science and Technology*. John Wiley & Sons, Inc., 2011.

[15] S. B. Kwon and K. W. Lee. Aerosol nanoparticles: Theory of coagulation. *Dekker Encyclopedia of Nanoscience and Nanotechnology*, 1:35–44, 2004.

[16] D. L Koch and J. Chun. Coagulation of monodisperse aerosol particles by isotropic turbulence. *Physics of fluids*, 17:–, 2005.

[17] William C. Hinds. *Aerosol Technology, Properties, Behavior and Measurement of Airborne Particles*. John Wiley & Sons, Inc., 1999.

[18] D. Pollard and P. Radchenko. Nonlinear least-squares estimation. *Journal of Multivariate Analysis*, 97(2):548–562, 2006.

[19] C. Roth, J. Gebhart, and W. Reisert. The production of high-concentrated monodisperse aerosols with variable size distributions. *Journal of Aerosol Science*, 23:185–188, 1992.

[20] J. O. Onyechi, G. Martin, and C. Marriott. The generation and properties of solid monodisperse aerosols of stearic acid and carnauba wax. *Animal research international*, 6(2):1028–1034, 2009.

[21] I. L. Mostinsky. Aerosols. *A-to-Z Guide to Thermodynamics, Heat and Mass Transfer, and Fluids Engineering*, 2010.

[22] J. N. Gence. Homogeneous turbulence. *Annual review of Fluid Mechanics*, 15:201–222, 1983.

[23] F. Stratmann, Th. Kauffeldt, D. Hummes, and H. Fissan. Differential electrical mobility analysis: A theoretical study. *Journal of Aerosol Science and Technology*, 26(4):368–383, 1997.

[24] W. Liu, B. Osmondson, O. Bischof, and G. Sem. Calibration of condensation particle counters. *SAE Technical Paper*, 2005-01-0189, 04 2005.

[25] Yogendra Singh, Julie Javier, Sheryl Ehrman, Martin Magnusson, and Knut Deppert. Approaches to increasing yield in evaporation/condensation nanoparticle generation. *Journal of Aerosol Science*, 33:1309–1325, 09 2002.

[26] Linda H. Schmoll, Sherrie Elzey, Vicki H. Grassian, and Patrick T. O'Shaughnessy. Nanoparticle aerosol generation methods from bulk powders for inhalation exposure studies. *Nanotoxicology*, 3(4):265–275, 2009.

[27] Igor Pujalte, Alessandra Serventi, Alexandra Noël, Denis Dieme, Sami Haddad, and Michèle Bouchard. Characterization of aerosols of titanium dioxide nanoparticles following three generation methods using an optimized aerosolization system designed for experimental inhalation studies. *Toxics*, 5:14, 07 2017.

[28] R. M. Rubsamen, S. J. Farr, and F. Silverstein. Patent number: Us5829436a, ventilation imaging using a fine particle aerosol generator, 1997.

[29] U. Backman. Studies on nanoparticle synthesis via gas-to-particle conversion. *VTT Publications*, 562:45–62, 2005.

[30] Y. Singh, J. Javier, S. H. Ehrman, M. Magnusson, and K. Deppert. Approaches to increasing yield in evaporation/condensation nanoparticle generation. *Journal of Aerosol Science*, 33(9):1309–1325, 2002.

[31] Nomura T., M. Alonso, Y. Kousaka, and E. Tenjiku. Simple model of aerosol particle formation by the evaporation–condensation method. *Journal of Colloid and Interface Science*, 231(1):107–113, 2000.

[32] J. M. Veranth, R. Gelein, and G. Oberdörster. Vaporization–condensation generation of ultrafine hydrocarbon particulate matter for inhalation toxicology studies. *Journal of Aerosol Science and Technology*, 37(7):603–609, 2003.

A Appendix

Measured aerosol flow values

Table 4: Aerosol flow for different experiments.

Experiment	Q_{aero} (lpm)	Experiment	Q_{aero} (lpm)
2017-08-29	1.07	2017-10-19	1.06
2017-08-31	1.07	2017-11-02	1.03
2017-09-01	1.06	2019-07-01	1.03
2017-09-04	1.05	2019-07-03/04	1.00
2017-09-11	1.04	2019-07-04/05	1.00
2017-09-25	1.07	2019-07-08/09	1.01
2017-09-26/27	1.09	2019-07-16	1.05
2017-10-03	1.06	2019-07-29	0.99
2017-10-11	1.03	2019-07-31	1.01
2017-10-12	1.02	2019-08-01	1.02
2017-10-18	1.05	2019-08-05	1.04

Samples of size distributions from experiments without cleaning
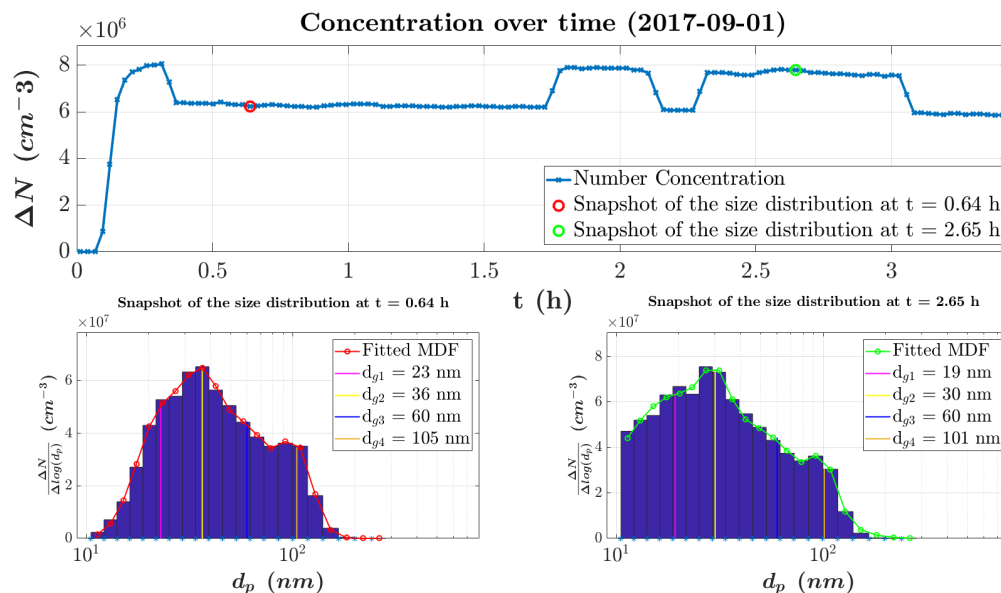
Figure 34: Concentration over time and snapshots of the size distributions and their fitted multimodal distribution function at two different times.
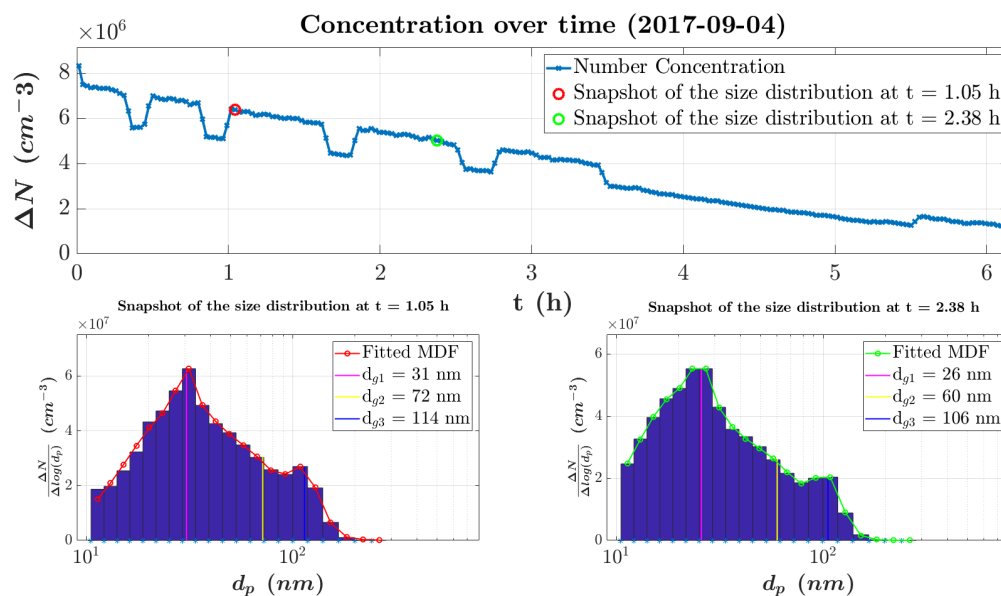
Figure 35: Concentration over time and snapshots of the size distributions and their fitted multimodal distribution function at two different times.
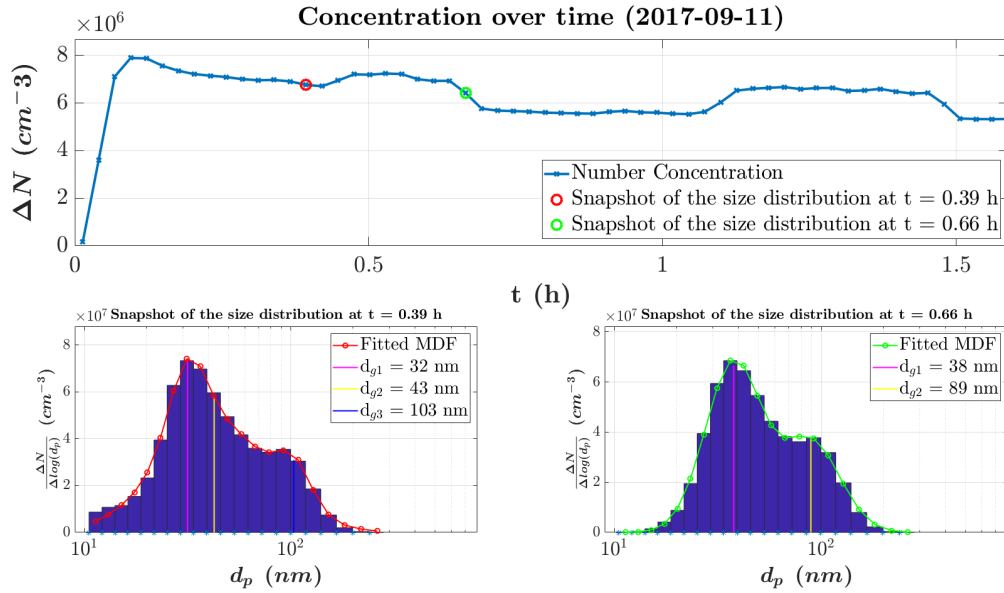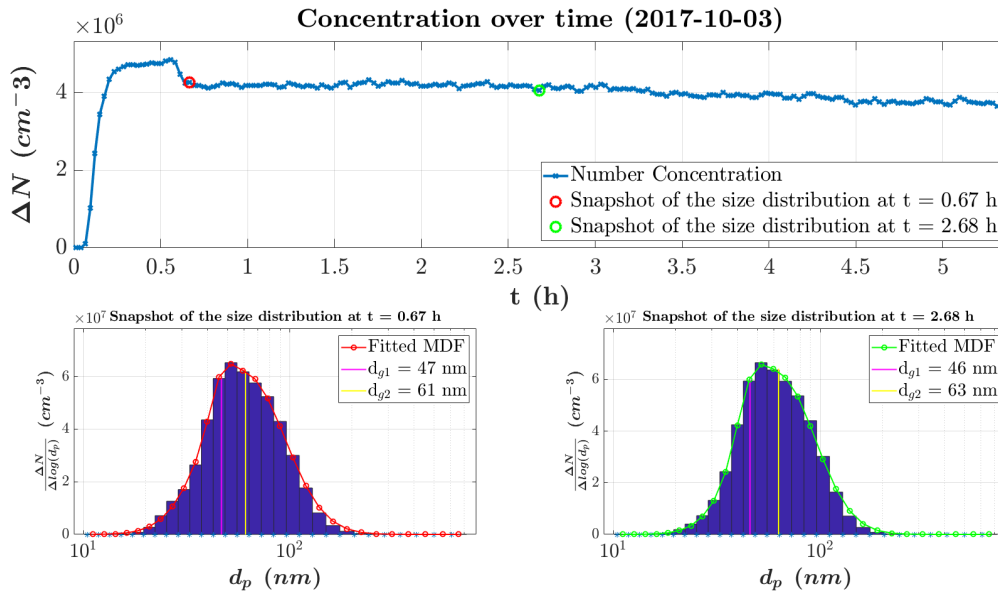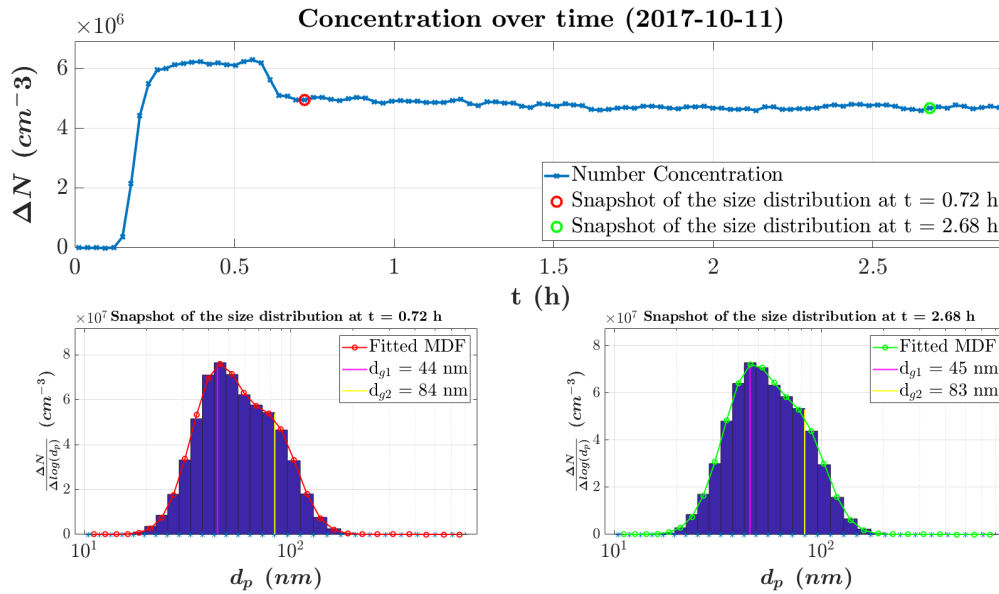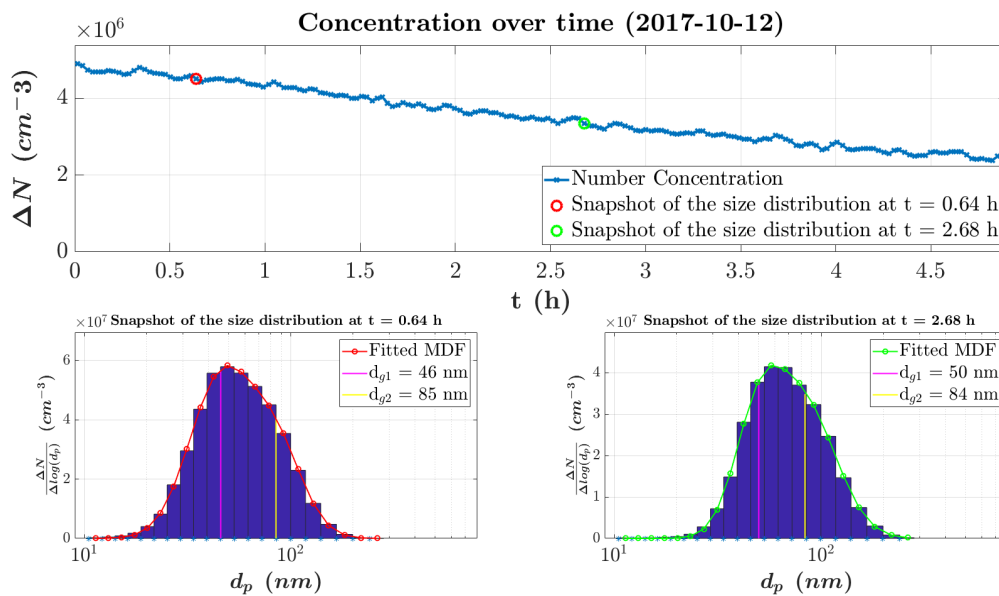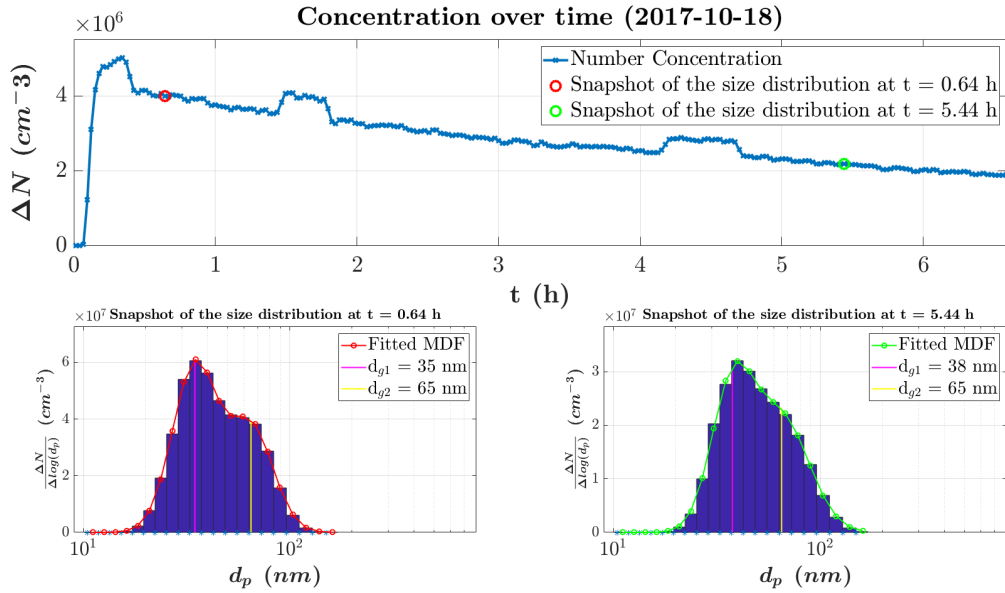
Figure 36: Concentration over time and snapshots of the size distributions and their fitted multimodal distribution function at two different times.
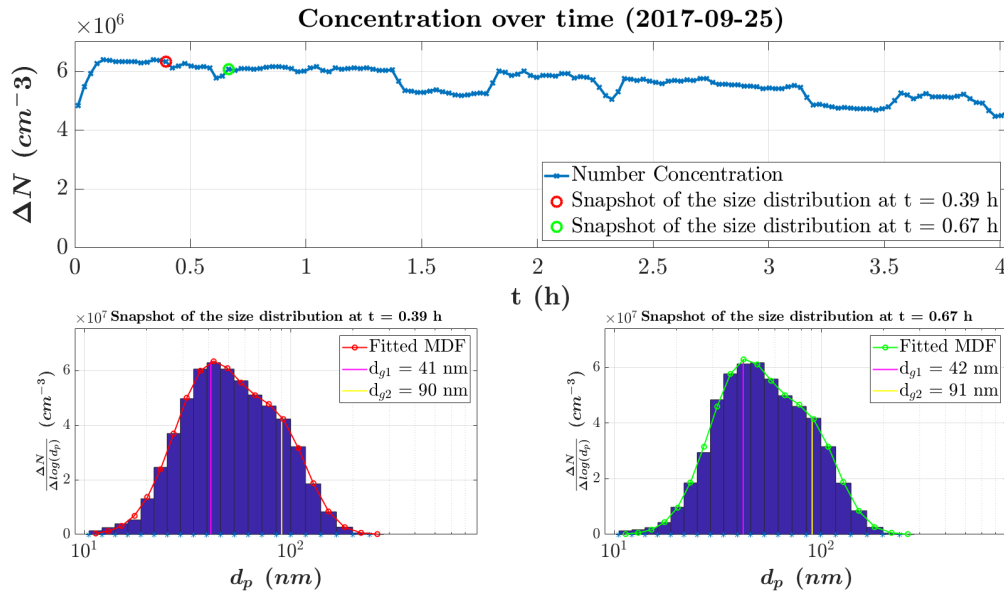
Figure 37: Concentration over time and snapshots of the size distributions and their fitted multimodal distribution function at two different times.
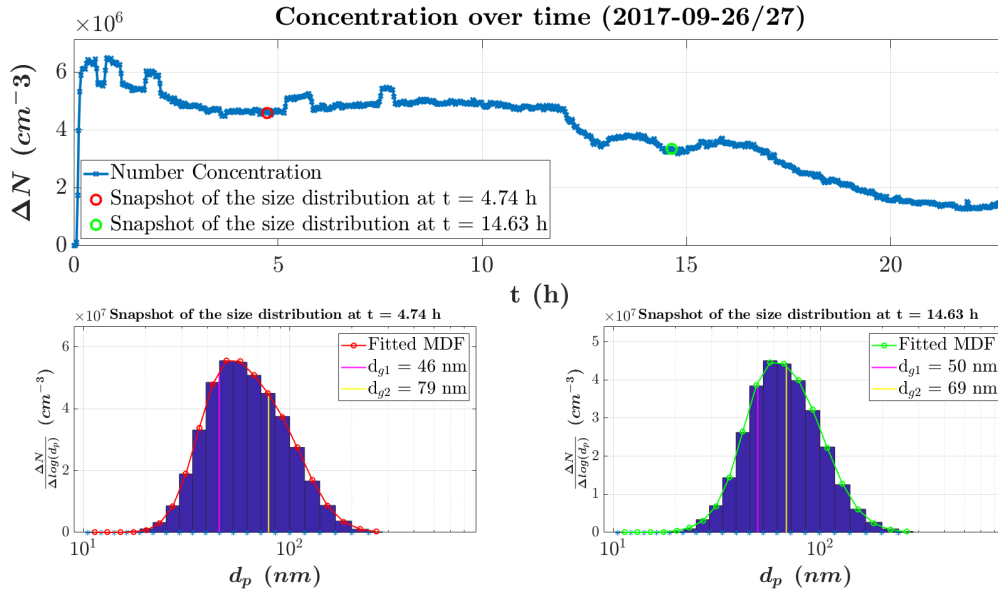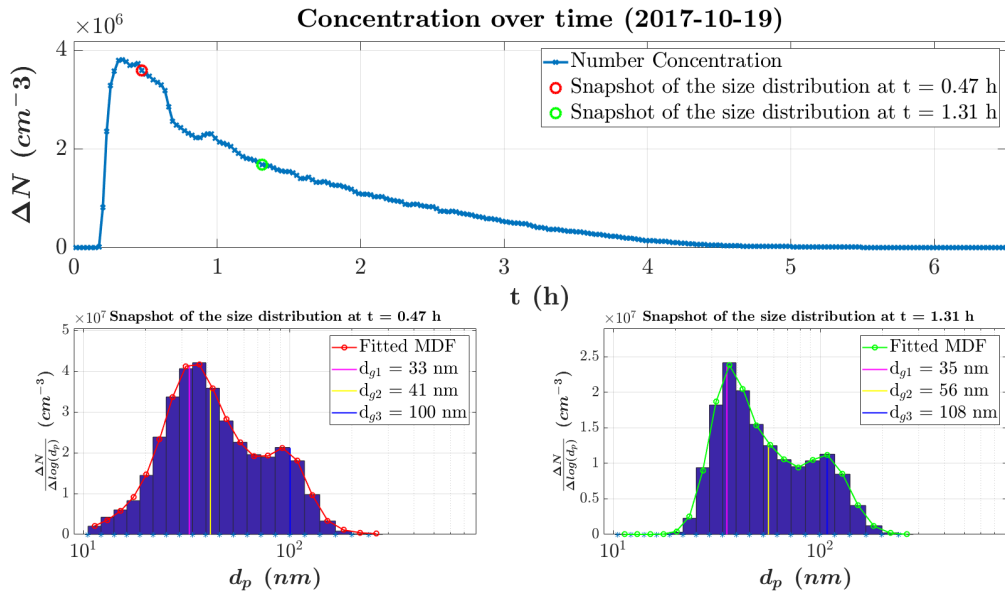
Figure 38: Concentration over time and snapshots of the size distributions and their fitted multimodal distribution function at two different times.
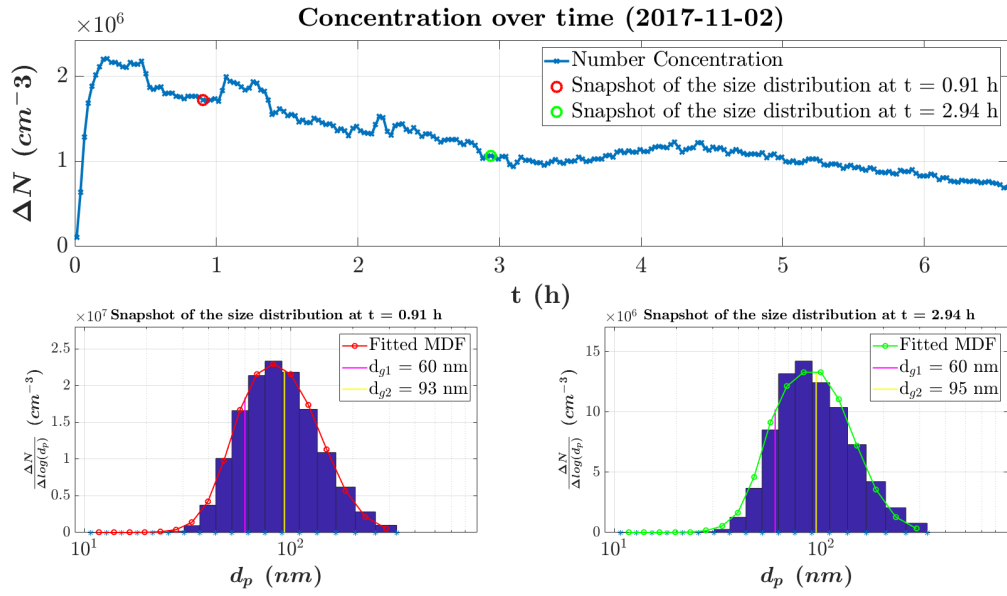

Figure 39: Concentration over time and snapshots of the size distributions and their fitted multimodal distribution function at two different times.

Samples of size distributions from experiments with cleaning

Figure 40: Concentration over time and snapshots of the size distributions and their fitted multimodal distribution function at two different times.

Figure 41: Concentration over time and snapshots of the size distributions and their fitted multimodal distribution function at two different times.
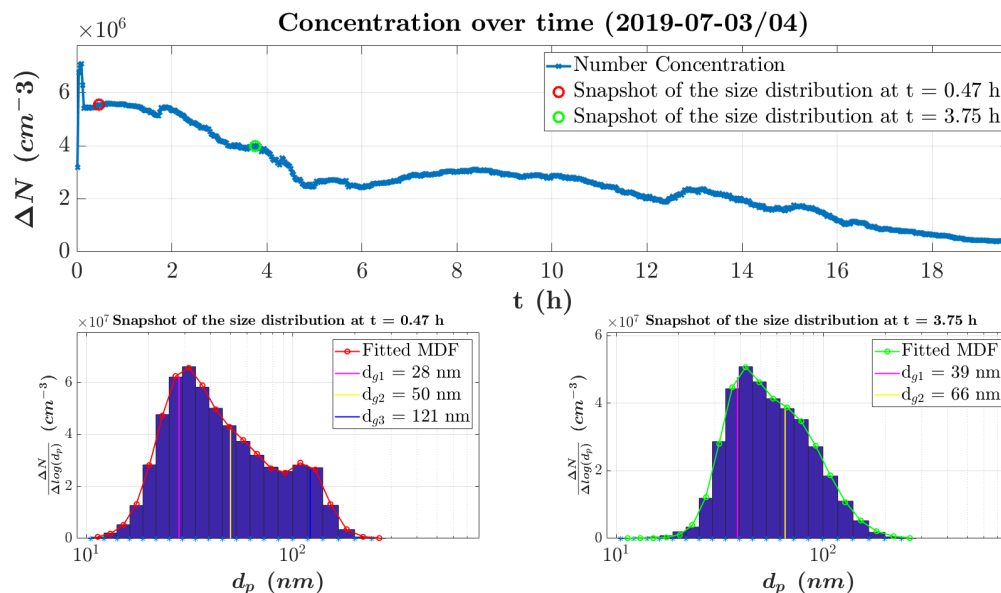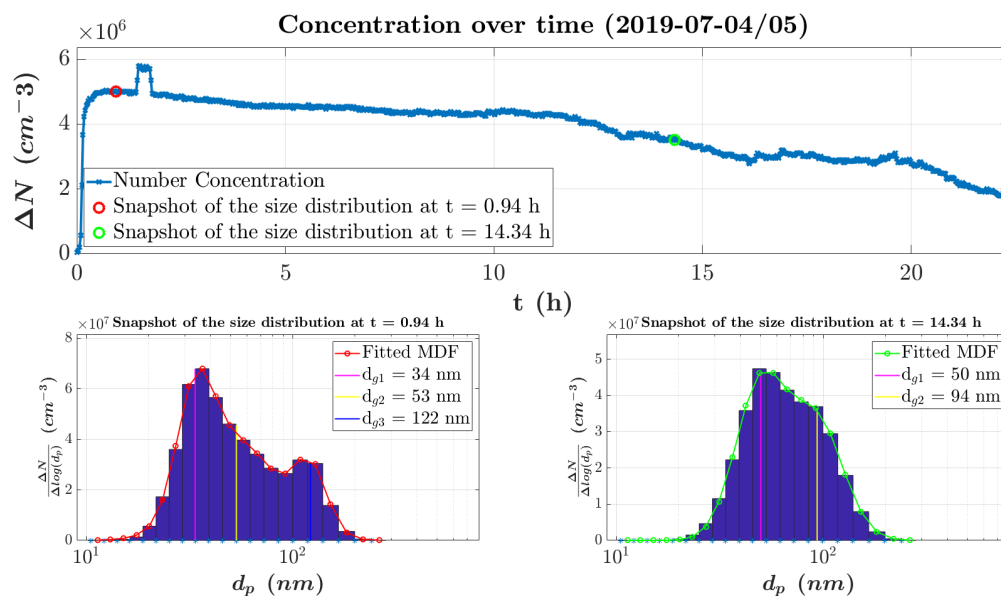
Figure 42: Concentration over time and snapshots of the size distributions and their fitted multimodal distribution function at two different times.

Figure 43: Concentration over time and snapshots of the size distributions and their fitted multimodal distribution function at two different times.

Figure 44: Concentration over time and snapshots of the size distributions and their fitted multimodal distribution function at two different times.
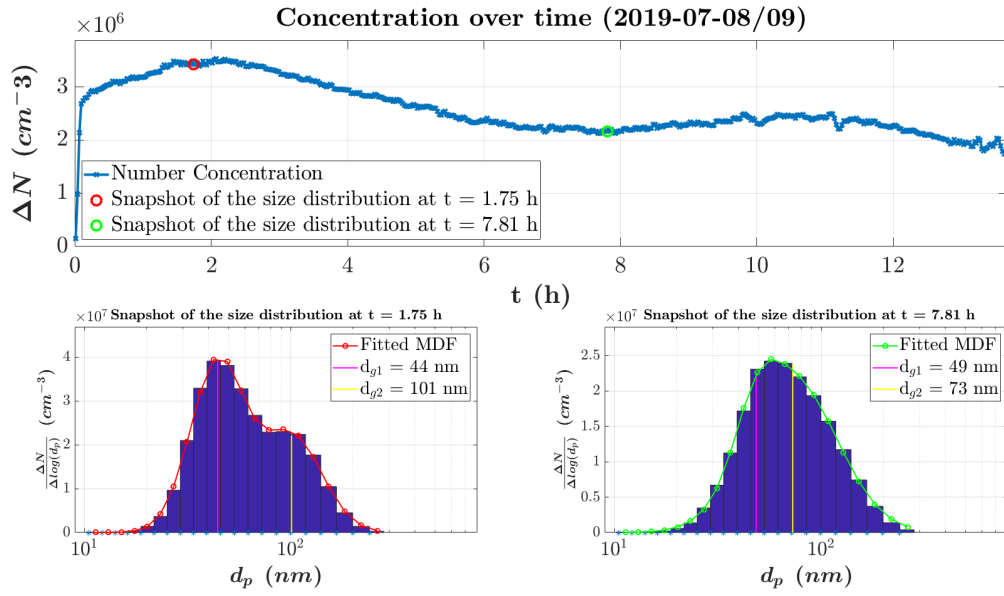
Samples of size distributions from long run experiments with cleaning

Figure 45: Concentration over time and snapshots of the size distributions and their fitted multimodal distribution function at two different times.

Figure 46: Concentration over time and snapshots of the size distributions and their fitted multimodal distribution function at two different times.

Figure 47: Concentration over time and snapshots of the size distributions and their fitted multimodal distribution function at two different times.
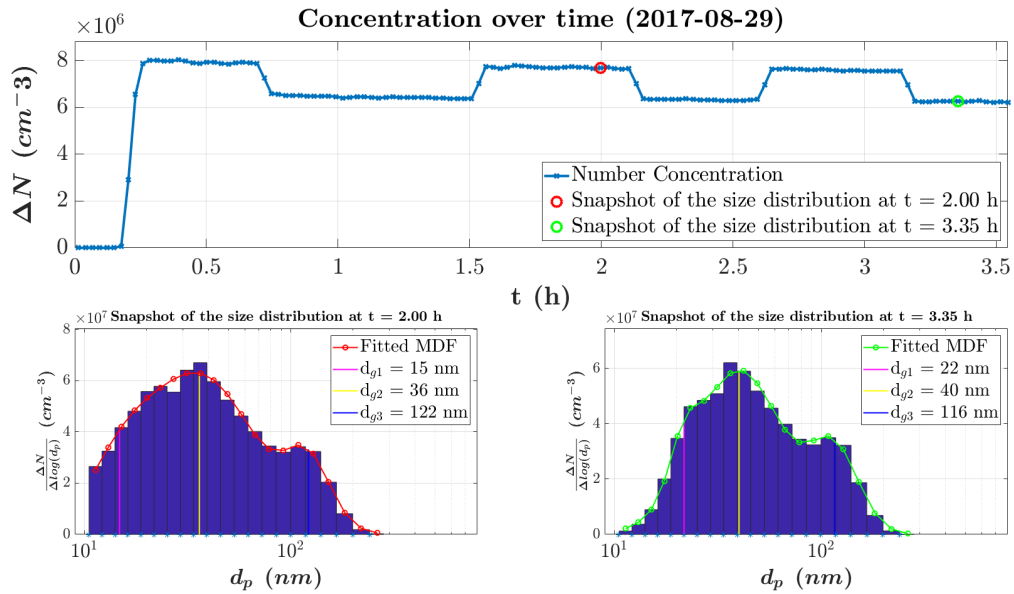
Samples of size distributions from test runs

Figure 48: Concentration over time and snapshots of the size distributions and their fitted multimodal distribution function at two different times.
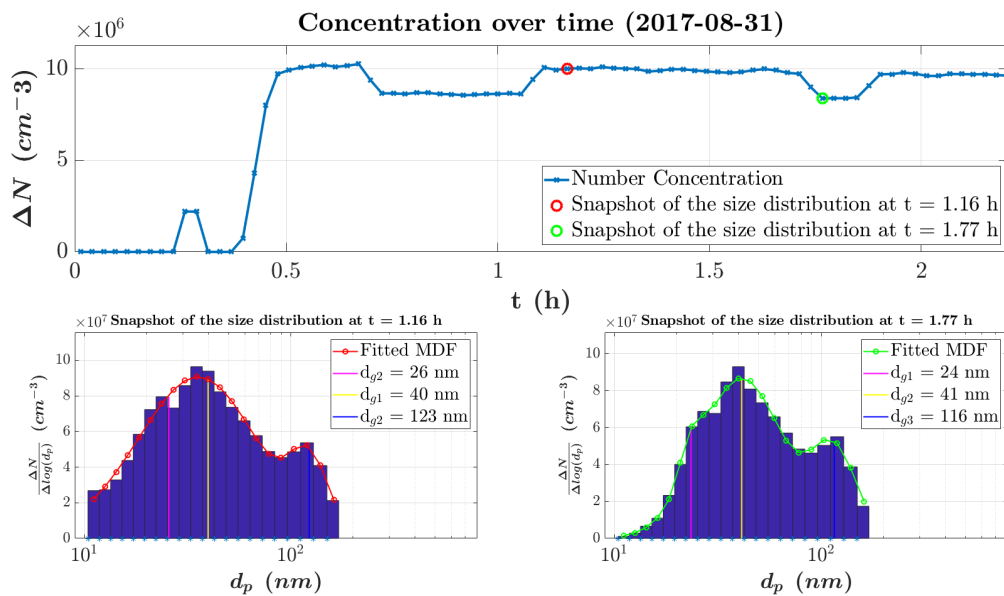

Figure 49: Concentration over time and snapshots of the size distributions and their fitted multimodal distribution function at two different times.
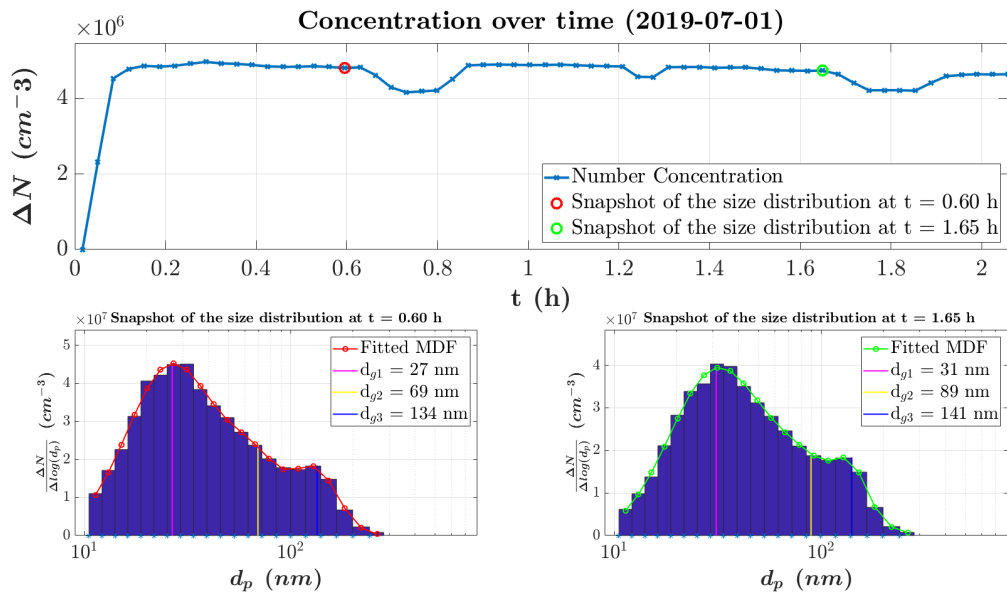
Figure 50: Concentration over time and snapshots of the size distributions and their fitted multimodal distribution function at two different times.